Materials Advances

ROYAL SOCIETY OF CHEMISTRY

PAPER

View Article Online
View Journal | View Issue

Cite this: *Mater. Adv.*, 2024, **5**, 4913

Control of spin on ferromagnetism and thermoelectric properties of K_2GeMnX_6 (X = Cl, Br, I) halide perovskites: emerging candidates for semiconductor spintronics and thermoelectric applications

Mudasir Younis Sofi, Mohd Shahid Khan and M. Ajmal Khan*

In this systematic report, *ab initio* simulations based on density functional theory (DFT) have been performed to examine the structural and elastic stability, electronic profile, and transport properties of K_2GeMnX_6 (X = Cl, Br, I) double halide perovskites. The structural optimization, evaluation of mechanical stability criteria, and assessment of the tolerance factor collectively confirm the stability of the halide perovskites in a cubic structure with $Fm\bar{3}m$ symmetry. The stability of the primary magnetic phase is established through minimization of total crystal energy at the behest of Birch–Murnaghan's equation across diverse magnetic phases. The ferromagnetic state is identified as the fundamental ground state, supported by positive Curie–Weiss constant values of 101 K for $K_2GeMnCl_6$, 100 K for $K_2GeMnBr_6$ and 90 K for K_2GeMnI_6. Additionally, the dynamic stability has been assessed through the calculation of phonon band structures utilising density functional perturbation theory (DFPT). The electronic band structures and density of states, obtained from both the generalized gradient approximation (GGA) and the TB-mBJ potential, designate a semiconducting ferromagnetic behavior characterized by a substantial spin-splitting gap, indicating their promising potential for semiconductor spintronics. The investigation into magnetism reveals values of $5\mu_B$ for each compound, primarily originating from the transition metal atom (Mn^{+2}). Also, the Curie temperature for each compound has been determined, with values reaching 710 K for $K_2GeMnCl_6$, 650 K for $K_2GeMnBr_6$, and 570 K for K_2GeMnI_6, ensuring exceptional stability of the ferromagnetic phase well beyond typical ambient conditions. The analysis of the transport properties of K_2GeMnX_6 (X = Cl, Br, I) double perovskites involved examining both the temperature and chemical potential dependencies of thermoelectric coefficients, specifically focusing on the Seebeck coefficient, electrical conductivity, and figure of merit. The significantly low thermal conductivity values of 2.2 K W mK^{-1} for $K_2GeMnCl_6$, 2 K W mK^{-1} for $K_2GeMnBr_6$, and 1.95 K W mK^{-1} for K_2GeMnI_6 highlight their potential for efficient waste heat recovery. Furthermore, with figure of merit (zT) values of 1.01, 1.00, and 0.99 at room temperature for $K_2GeMnCl_6$, $K_2GeMnBr_6$, and K_2GeMnI_6 double halide perovskites respectively, these materials exhibit promising potential for both thermoelectric and renewable energy applications. The study also investigates the optical and dielectric properties, unveiling substantial absorption and photoconductivity in the visible and UV regions, thereby endorsing their potential as promising lead-free candidates for optoelectronics and solar cell applications. The comprehensive investigation overall lends support to the potential use of these materials in semiconductor spintronics, thermoelectric technology, optoelectronics, and other emerging technological domains.

Received 21st December 2023,
Accepted 25th April 2024

DOI: 10.1039/d3ma01160g

rsc.li/materials-advances

1. Introduction

The advancements in spintronics and quantum computing technology have greatly increased the speed of memory storage, endowing it with versatile capabilities. This evolving field aims to minimize the size of magnetic chips and enhance memory speed by utilizing both electron spin and charge.[1,2] Advanced spintronic technology has achieved notable milestones, particularly in non-volatile magnetic random-access memory.[3,4] The versatility of these advancements extends to electronic devices, offering benefits such as cost-effectiveness, faster data speed,

Department of Physics, Jamia Millia Islamia, New Delhi-110025, India.
E-mail: majkhan@jmi.ac.in

and reduced power consumption.[5,6] Additionally, contemporary quantum technology exploits electronic spin states in digital displays, departing from conventional charge-centric electronic operations. The landmark discovery of giant magnetic resistance (GMR) in 1998 played a pivotal role in advancing this technology.[7] By harnessing electron spin, GMR induces a notable disparity in the resistance of different magnetic layers when subjected to external magnetic fields. Consequently, the interplay between electronic charge and spin facilitates the creation of low-powered, high-speed, non-volatile, and nano-sized memory solutions.[8,9] The current scientific achievements in spintronics technology have led to improvements in magneto-resistive random-access memory (MRAM), magnetic sensors, magnetic valves, read heads for magnetic hard drives, and the giant magneto-resistive effect (GMR). Materials characterized by high spin polarization (SP) have emerged as suitable candidates for application in spintronics technology. Despite significant efforts in exploring spintronic materials, achieving 100% spin-polarized carriers at room temperature (RT) remains a major challenge. So far, numerous spintronic materials have been investigated, including spinels ($NiFe_2O_4$),[10] europium chalcogenides (EuO, EuS),[11,12] double perovskite oxides (Bi_2FeCrO_6, Sr_2CrWO_6),[13,14] and Heusler compounds (CoVTiAl, CoVZrAl).[15] However, the limited quantity of spin-polarized carriers and low Curie temperature present critical obstacles for realizing their RT spintronics.[16] Prerequisites for realizing 100% spin-polarized carriers at RT involve nondegenerate electronic band structures with substantial spin splitting and a Curie temperature (T_C) surpassing RT.[16] While pristine halide perovskites exhibit excellent optoelectronic properties, they generally lack magnetism. Náfrádi *et al.*[17] have documented the observation of weak magnetism in Mn-doped $CH_3NH_3PbI_3$, indicating a potential avenue for halide perovskite based spintronics. However, the limited spin splitting of less than 0.2 eV and the low Curie temperature of less than 15 K in their devices must be significantly enhanced before achieving room temperature operation in spintronics. In contrast, the pursuit of intrinsic ferromagnetic semiconductors, unaided by any doping strategy, holds considerable potential for application in spintronics. Double perovskite oxides have garnered extensive attention in spintronic calculations, attributed to their straightforward crystal structures, facile modelling, a diverse array of elemental constituents, and the capacity for tuning electronic and magnetic properties. Despite these advancements, the magnetism of double perovskite halides (DPHs) remains largely unexplored to date. Recently *Cai et al.*[18] investigated a novel class of double halide perovskites, exploring their essential characteristics in terms of stability, electronic profiles, and Curie temperature. The findings indicated that these materials exhibit both structural and dynamic stability, while displaying ferromagnetic semiconductor behavior with substantial spin splitting and significant Curie temperatures. Consequently, these materials were identified as compelling materials for semiconductor spintronics applications. Beyond their relevance in semiconductor spintronics, these halide double perovskites (DPHs) display an exceptional feature of ultra-low thermal conductivity.[19] This distinctive property arises from the placement of heavier elements within the structural framework, serving as substantial rattlers and introducing lattice anharmonicity. As a result, these materials are anticipated to demonstrate a favourable thermoelectric response. In our recent study, we documented notable thermoelectric figure of merit (zT) values of 1.00 and 0.99 for $K_2GeNiBr_6$ and K_2GeNiI_6 halide double perovskites, respectively.[20]

Motivated by these intriguing characteristics, we designed a novel class of double halide perovskites, systematically exploring their structural, magneto-electronic, Curie temperature, and thermoelectric properties in detail. The outcomes of our calculations on spin-polarized band structures and density of states distinctly indicate the manifestation of ferromagnetic semiconductor behaviour in K_2GeMnX_6 (X = Cl, Br, I) compounds, coupled with a notably high Curie temperature. Consequently, these materials exhibit promising attributes as emerging candidates for semiconductor spintronics applications. Furthermore, we conducted computations encompassing both temperature variations and chemical potential dependency to assess transport parameters such as the Seebeck coefficient, electrical conductivity, and the figure of merit (zT). The elevated room temperature zT values, stemming from the exceptionally low thermal conductivity and higher Seebeck coefficient values, endorse the suitability of these materials for application in thermoelectric technology. To forecast the comprehensive physical (structural, electronic, mechanical, phonon, thermodynamic, optical) and thermoelectric properties, the paper is structured as follows.

2. Theoretical models

The computations have been exclusively conducted utilizing the Wein2k simulation code and integrated packages associated with it.[21] The iterative solution of the Kohn–Sham equation is facilitated by the generalized gradient approximation (GGA).[22] Acknowledging GGA's limitations in accurately representing electronic structures of highly correlated d/f electron systems, the mBJ potential has been introduced to enhance the scrutiny of electronic structures, leading to the utilization of GGA+mBJ.[23] In the FP-LAPW approach, the unit cell volume undergoes subdivision into muffin tin spheres, strategically centered at Wyckoff positions (4a, 4b, 8c, and 24e) corresponding to occupied atoms and interstitial spaces. Muffin tin radii (R_{MT}) are carefully chosen to address charge leakage considerations while optimizing computational efficiency. A linearized augmented plane wave basis set is employed, ensuring atomic like character within MT spheres and a Bloch wave nature in interstitial spaces. The atomic wave functions within spheres extend to l_{max} = 10, while the plane wave cutoff condition is defined by $R_{MT}K_{max}$ = 7. Self-consistent calculations are deemed complete when the integrated charge difference between successive cycles is less than 0.0001e and the corresponding energy difference is less than or on the order

of 0.0001 Ry. The Brillouin zone is discretized into 1000 *k*-points for the determination of magneto-electronic structures and elastic constants. To evaluate the mechanical stability, the Thomas Charpin cubic elastic package has been employed within the framework of the GGA-PBE approach.[24] Thermodynamic properties were acquired through the Gibbs2 package,[25] seamlessly integrated with the Wien2k code. The thermoelectric coefficients have been deduced using Boltzmann transport theory in conjunction with the rigid-band model and the constant-scattering time approximation (CSTA).[26] To enhance computational accuracy, the determination of transport coefficients has been executed using a denser mesh comprising 100 000 *k*-points.

3. Results and discussion

The employment of density functional theory calculations, utilizing two approximation schemes, namely PBE-GGA and TB-mBJ, has been discussed for the predictive analysis of diverse physical properties concerning the novel halide perovskites K_2GeMnX_6 (X = Cl, Br, I).

3.1. Crystallographic structures and magnetic ground states

Crystal structures are characterized by internal structural parameters, which can be determined using experimental methods or computational approaches. Experimentalists rely on techniques such as X-ray diffraction (XRD) and Fourier-transform infrared spectroscopy (FTIR) approaches to elucidate and determine the crystal structure. In a computational context, one can predict the stability and ground state structure of a material by minimizing the crystal energy with respect to its volume. The determination of phase stability of K_2GeMnX_6 (X = Cl, Br, I) materials involves a computational approach, wherein the total energy is computed as a function of varying volume using distinct magnetic configurations. The optimization plots, illustrated in Fig. 1, affirm the stability of K_2GeMnX_6 in the cubic $Fm\bar{3}m$ space group. The energy–volume plot for the ferromagnetic phase reveals a minimum energy corresponding to the optimum volume. At this volume, the lattice constants are determined to be 10.35 Å for $K_2GeMnCl_6$, 10.61 Å for $K_2GeMnBr_6$ and 11.75 Å for K_2GeMnI_6 compounds. The lattice constant increases as the halide ion X (ranging from Cl to I) progresses, which can be attributed to variances in atomic sizes and interatomic interactions within the crystal lattice. Given the larger atomic radius of iodine (I) compared to bromine (Br) and chlorine (Cl), the lattice parameter of K_2GeMnI_6 is inherently larger, reflecting the influence of atomic dimensions on the lattice structure. The obtained values for the lattice constant are consistent with other published findings.[18,20] The other equilibrium parameters defining the ground state, as determined through the minimization of total energy, are outlined in Table 1. It is worth noting that the generalized gradient approximation (GGA-PBE) yields a lattice parameter value that exhibits the closest agreement with experimental findings.

The stability of the cubic phase is further substantiated by the computation of the tolerance factor. The tolerance factor can be derived from either ionic radii,[18] $t_r = \frac{0.71(r_K + r_X)}{r_{avg} + r_X}$, or bond lengths, $t_b = \frac{0.71\langle K - X\rangle}{\langle M' - X\rangle_{avg}}$. Here r_K and r_X are the ionic radii of K and Cl/Br/I atoms, while r_{avg} is the average ionic radii of Ge and Mn atoms, respectively. Besides, $\langle$K–X$\rangle$ signifies the interatomic distance between potassium (K) and bromine (Br)/iodine (I) atoms, whereas $\langle M'–X\rangle_{avg}$ indicates the average of germanium (Ge)–X and manganese (Mn)–X bond distances. The acquired values, as presented in Table 1, lie within the range of $0.81 < t < 1.11$ for the specified materials, affirming their stability in the cubic structure. Within the unit cell, K is surrounded by a cage of twelve Cl/Br/I atoms, as depicted in Fig. 2. Meanwhile, Ge and Mn exhibit a coordination number of six with Cl/Br/I atoms, placing them in an octahedral environment of Cl/Br/I anions. The bond lengths and tolerance factor collectively contribute to determining the stable phase of these double halide perovskites.

In the pursuit of theoretically evaluating the potential for experimental synthesis and determining the resistance of these compounds to spontaneous decomposition into other binary or elemental phases, we computed the enthalpy of formation energy, denoted as[27] $\Delta H = \frac{1}{10}\left[E_{total}^{K_2GeMnX_6} - (2E_K + E_{Ge} + E_{Mn} + 6E_X)\right]$, where $E_{total}^{K_2GeMnX_6}$ represents the equilibrium energy of the unit cell and E_K, E_{Ge}, E_{Mn}, and E_X illustrate the calculated DFT energies of potassium (K), germanium (Ge), manganese (Mn), and chlorine/bromine/iodine (Cl/

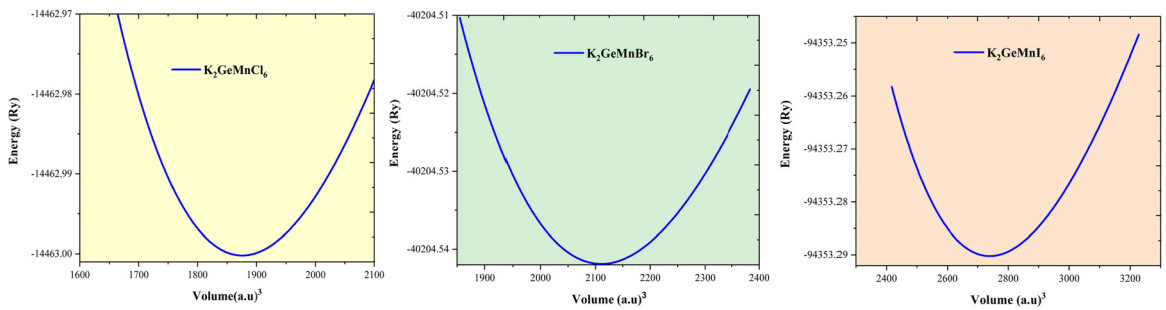

Fig. 1 Variation in total energy against unit cell volume for K_2GeMnX_6 (X = Cl, Br, I) determined *via* the GGA-PBE functional scheme.

Table 1 Computed values for the optimised lattice parameter (a_0 in Å), bulk modulus (B in GPa), pressure derivative of bulk modulus (unitless), ground state energy (E_0 in eV), tolerance factor (t_r; t_b), enthalpy of formation (ΔH in eV) and cohesive energy (E_C in eV) of K_2GeMnX_6 (X = Cl, Br, I) halide perovskites

Configuration	Phase	a_0	Previous works	B	B'_0	E_0	t_r	t_b	ΔH	E_C
$K_2GeMnCl_6$	FM	10.35	10.53[18]	29.33	4.48	−196696.82	0.95	1.00	−2.34	32.12
$K_2GeMnBr_6$	FM	10.93	11.10[18]	24.56	4.84	−546781.75	0.94	1.00	−1.54	27.52
K_2GeMnI_6	FM	11.75	11.92[18]	19.40	4.80	−1283204.74	0.92	1.00	−1.17	22.19

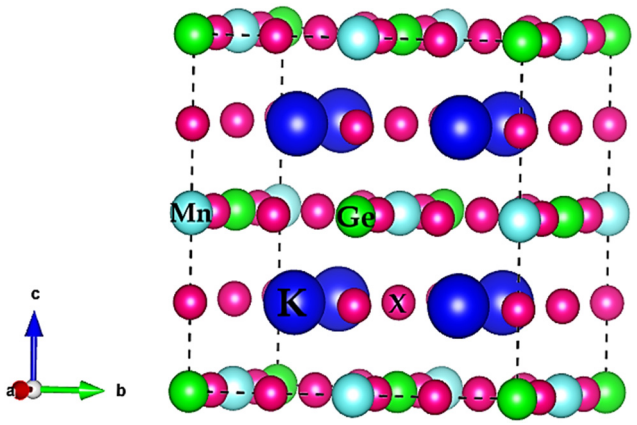

Fig. 2 Crystal structure of K_2GeMnX_6 (X = Cl, Br, I) double halide perovskites.

Br/I) atoms in their stable elemental crystal structures. The negative values of ΔH obtained, as depicted in Table 1, signify the practical feasibility of experimental synthesis and production of these materials.

Also, we computed the cohesive energy of the materials using the formula[27] $E_{Coh}^{K_2GeMnX_6} = [2E_K + E_{Ge} + E_{Mn} + 6E_X] - E_{total}^{K_2GeMnX_6}$, where $E_{total}^{K_2GeMnX_6}$ is the equilibrium energy of the unit cell and E_K, E_{Ge}, E_{Mn}, and E_X are the energies of the isolated atoms K, Ge, Mn, and X (Cl, Br, and I), respectively. The positive cohesive energy values, detailed in Table 1, further validate the interatomic stability of these materials.

Additionally, as per the OQMD database, the energy above hull (E_{Hull}) for $K_2GeMnCl_6$ and $K_2GeMnBr_6$ is reported as 0.03 and 0.036 per atom, respectively, thus reaffirming their potential feasibility for experimental synthesis.[28] Furthermore, we utilized density functional theory (DFT) simulations to generate X-ray diffraction (XRD) patterns for these compounds in the cubic configuration ($Fm\bar{3}m$), as illustrated in Fig. 3. These simulated patterns offer valuable guidance for potential experimental investigations into the structural properties of these materials.

3.2. Phonon band structure

To comprehend the dynamic stability and vibrational Raman spectroscopy of crystalline solids, it is essential to explore the concept of phonon frequency dispersion. The application of density functional perturbation theory (DFPT) within the Quantum Espresso pseudopotential framework has been utilized to evaluate the dynamical stability of the specified materials at operational temperatures.[29] In the realm of dynamic stability, a system is deemed stable when its phonon frequencies are real and positive; conversely, negative or imaginary frequencies indicate instability. The phonon dispersion bands depicted in Fig. 4 demonstrate the absence of negative phonon frequencies, thus confirming the dynamic stability of the materials. The phonon bands display three acoustical modes and twenty-seven optical modes, in line with the presence of ten atoms in the primitive unit cell of these materials. At the reciprocal space Γ-point (k = 0), three acoustic branches with zero frequency converge, identified as longitudinal acoustic (LA) and transverse acoustic (TA) modes. Additionally, the 27 optical modes with non-zero frequencies include Raman, infrared, and silent modes, categorized according to factor theory. The group velocity of a phonon, expressed by $v_g = \frac{d\omega}{dk}$, reflects the slope of associated branches. Optical branches exhibit a flat curvature, signifying low group velocity, while longitudinal

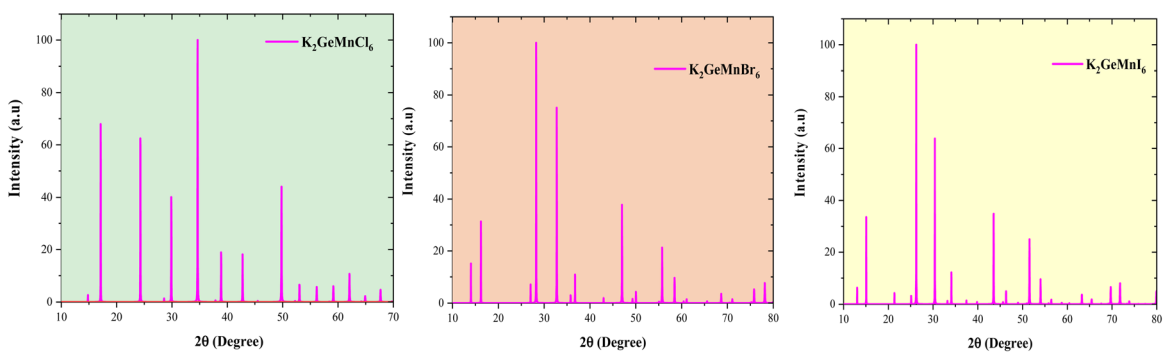

Fig. 3 DFT-simulated XRD patterns of K_2GeMnX_6 (X = Cl, Br, I) halide perovskites.

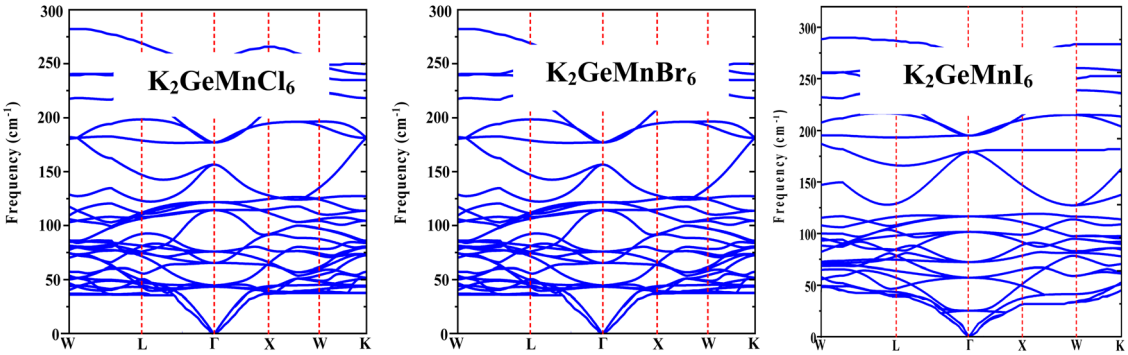

Fig. 4 Phonon band structure of K_2GeMnX_6 (X = Cl, Br, I) halide perovskites.

acoustical branches, characterized by linear variation, demonstrate substantial group velocity. Hence, these acoustical modes significantly contribute to thermal conduction due to their high group velocity, impacting the lattice thermal conductivity of a material.

3.3. Thermodynamic vibrational properties

The investigation into thermodynamic vibrational functions, which encompass vibrational contributions, is aimed at comprehending phenomena such as variations in vibrational internal energy (E), vibrational Helmholtz free energy (A), vibrational entropy (S_v), and specific heat at constant volume (C_v) relative to temperature (T). The quasi-harmonic Debye model is frequently employed for predicting these thermodynamic properties.[30,31] As per this model, the equations for vibrational Helmholtz free energy (A), Debye temperature (θ_D), vibrational entropy (S_v), and specific heat at constant volume (C_v) are provided as follows:

$$A_{\mathrm{Vib}}\left(\theta(V);\quad T = nk_{\mathrm{B}}T\frac{9\theta_D}{8T} + 3\ln\ 1 - e^{\frac{\theta_D}{T}} - D\left(\frac{\theta_D}{T}\right)\right)$$

$$\theta_D\frac{h}{K_{\mathrm{B}}}\left(6\pi^2V^{\frac{1}{2}}N\right)^{\frac{1}{3}}f(v)\sqrt{\frac{B_s}{M}}$$

$$S_{\mathrm{V}} = nk_{\mathrm{B}}T\left[4D\left(\frac{\theta_D}{T}\right) - 3\ln\ 1 - e^{\frac{\theta_D}{T}}\right]$$

$$C_{\mathrm{V}} = 3nk\left(4D\frac{\theta_D}{T} - \frac{3\theta_D/T}{e\theta^{D/T}}\right)$$

Here, n symbolizes the count of atoms per formula unit, k_B denotes the Boltzmann constant, B_s represents the adiabatic bulk modulus, M signifies the molecular mass per unit cell, and D stands for the Debye integral. Herein, we have investigated the fluctuations in vibrational thermodynamic functions concerning temperature, specifically focusing on variations in internal energy, Helmholtz free energy, vibrational entropy, and specific heat at constant volume.

We commence by examining vibrational internal energy (E), admitting the well-known phenomenon that sustained heat influx leads to an escalation in the kinetic energy of constituent atoms, thereby increasing atomic vibrations and consequently elevating vibrational internal energy. The variation in vibrational internal energy (E) with temperature (T), as depicted in Fig. 5(a), reveals a linear increase of E relative to T, indicating a corresponding rise in the system's enthalpy. The observed trend in vibrational Helmholtz free energy (A), illustrated in Fig. 5(b), exhibits a decrease in A with increasing T, progressing from Cl to I. This trend confirms that the thermal energy available for performing useful work reaches its maximum for $K_2GeMnCl_6$ and diminishes as X descends down the group. The level of intrinsic disorder within the system, quantified as entropy (S_v), demonstrates an increase as we progress down the periodic table group from Cl to I. This trend is attributed to the expanding atomic size, facilitating greater potential orientation for subatomic particles. The calculated S_v, as depicted in Fig. 5(c), emphasizes that the thermodynamic potential or thermal energy unavailable for performing useful work follows the order (X = I > Br > Cl) for K_2GeMnX_6 compounds. Moreover, S_v increases with temperature (T), indicating an augmentation in thermally accessible vibrational states.

In the domain of thermodynamics and statistical analyses,[32–34] heat capacity (C_v) assumes critical importance in understanding lattice vibrational characteristics. The behavior of the C_v plot delineates into two distinct regimes, as elucidated in Fig. 5(d). Initially, when temperature (T) significantly undershoots the Debye temperature (θ_D), it conforms to a specific relationship $C_V = \frac{12}{5}\pi^4 nR - \left(\frac{T}{\theta_D}\right)^3$. Conversely, at high temperatures ($T \gg \theta_D$) the curve approximates the expression $C_V \cong 3nR$, aligning with Dulong–Petit's limit[35]. Here, n denotes the number of atoms per formula unit, R represents the universal gas constant (approximately 8.314 J K^{-1} mol^{-1}), and θ_D stands for the Debye temperature at 0 K. The determined values for the Debye temperature (θ_D), the zero-point energy (E_0) expressed in kilojoules per mole, and the Gruneisen parameter γ (dimensionless) are tabulated in Table 2.

The analysis of the specific heat (C_v) plot portrayed in Fig. 5(d) elucidates the adherence of K_2GeMnX_6 (Cl, Br, I) compounds to the aforementioned principles. Remarkably, at temperatures (T) notably below the Debye temperature (θ_D), the observed rise in C_V correlates directly with T^3, confirming compliance with Debye's low-temperature specific heat law,

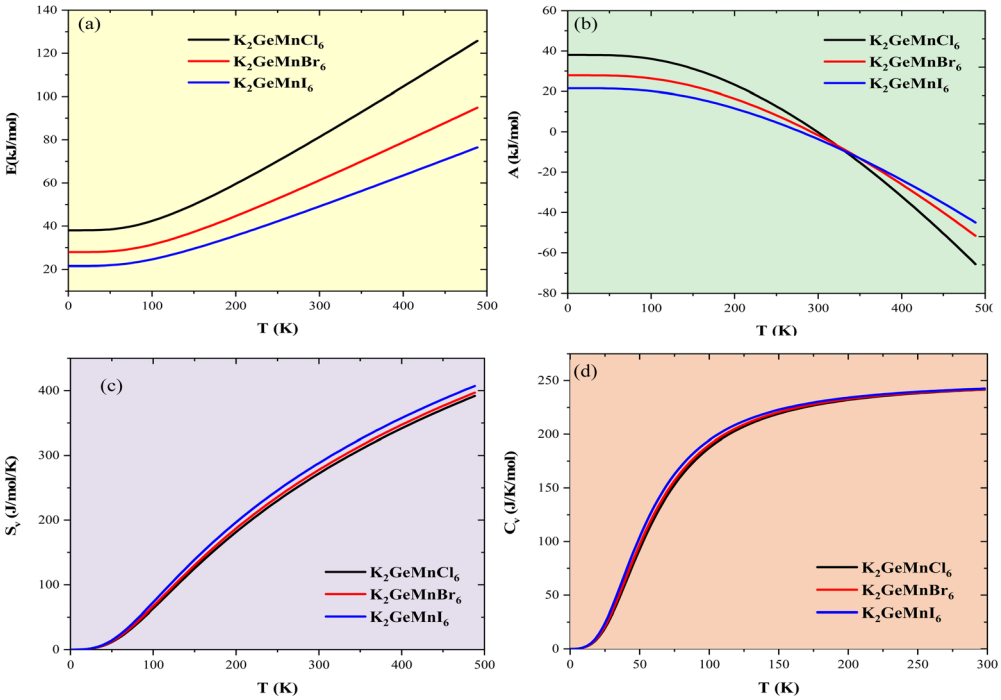

Fig. 5 Thermodynamic vibrational functions for K_2GeMnX_6 halide perovskites: (a) vibrational internal energy (E), (b) vibrational Helmholtz free energy (A), (c) vibrational entropy (S_v) and (d) specific heat (C_V) against a selected range of temperature.

commonly known as Debye's T^3 law. Conversely, at temperatures significantly surpassing θ_D, C_V remains nearly constant across all considered systems, approaching the Dulong–Petit limit, thereby indicating that our computational outcomes at elevated temperatures align with the classical thermodynamics embodied by the Dulong–Petit law.[35] The tabulated values of θ_D provided in Table 2 unveil a distinct descending trend following the sequence $K_2GeMnCl_6 > K_2GeMnBr_6 > K_2GeMnI_6$. This trend is attributed to compounds with heavier atoms displaying a reduced average velocity of sound (V_{av}), stemming from an increase in density. Furthermore, the dimensionless Gruneisen parameter (γ), computed as $\gamma = \frac{3(1+\varepsilon)}{2(2-\varepsilon)}$, serves as an insightful metric for predicting the anharmonic properties of the solid material. Remarkably, this parameter exhibits noteworthy consistency across all examined compounds, suggesting a uniform trend in thermodynamic properties for the scrutinized perovskites (K_2GeMnX_6). This consistency implies that these compounds are expected to demonstrate coherent thermodynamic behavior.

Table 2 Computed values for the Debye temperature (θ_D) measured in Kelvin, zero point energy (E_0) expressed in kilojoules per mole, and the Gruneisen parameter (γ) (dimensionless)

Parameter	θ_D	E_0	γ
$K_2GeMnCl_6$	406	39	2.01
$K_2GeMnBr_6$	300	28	2.07
K_2GeMnI_6	230	21	2.10

3.4. Mechanical stability

The comprehensive examination of structural properties provides additional insights into the mechanical characteristics of the materials. Furthermore, the arrangement of atoms within the structure holds significant importance in determining the material's resistance to external forces, thereby defining its mechanical stability. The assessment of mechanical stability serves as a crucial roadmap for industrial and technological applications. For the given perovskites, we ascertained elastic constants using the volume and energy approach, while maintaining tetrahedral and rhombohedral distortions within the cubic elastic package.[24] The eigenvalues of the elastic constant matrix for K_2GeMnX_6 (X = Cl, Br, I) halide perovskites, detailed in Table 3, exhibit positivity and adhere to the Born stability conditions[36] ($C_{11} > 0$, $C_{12} > 0$, $C_{44} > 0$, $C_{11} + 2C_{12} > 0$). This affirmation emphasizes the stability of double perovskites in the symmetric cubic phase ($Fm\bar{3}m$). The calculated elastic constants not only provide insights into the mechanical stability but also facilitate the analysis of various elastic parameters. Parameters like elastic moduli (bulk, shear, and Young)[37–39] are derived from elastic constants through mathematical relations reported elsewhere,[40] with the outcomes detailed in Table 3. The Young's modulus (Y), reflecting the stiffness of the alloy, is complemented by the bulk modulus (B), which inversely determines the resistance to volumetric deformation. The fracture strength, directly influenced by the bulk modulus, correlates with the material's resistance to volumetric changes. Shear modulus (G), indicating the resistance to plastic deformation, implies that lower G-values facilitate easier modulation of the alloy. The elastic moduli for these double perovskites follow the

Table 3 Intended second order elastic constants C_{11}, C_{12}, and C_{44} (GPa); bulk modulus B (GPa); shear modulus G (GPa); Young's modulus Y (GPa); Poisson's ratio ν; B/G ratio; Cauchy's pressure (C_{12}–C_{44}); Kleinman's parameter (ξ); Zener anisotropic constant (A_Z); and universal anisotropic constant (A_U) for K_2GeMnX_6 (X = Cl, Br, I) double halide perovskites

Parameter	C_{11}	C_{12}	C_{44}	B	G	Y	ν	B/G	C_{12}–C_{44}	ξ	A_z	A_U
$K_2GeMnCl_6$	57.01	16.08	9.83	29.72	16.46	47.03	0.27	1.80	6.25	0.43	0.48	0.30
$K_2GeMnBr_6$	45.89	14.34	6.13	24.85	9.04	24.18	0.33	2.74	8.21	0.45	0.37	0.25
K_2GeMnI_6	30.05	13.94	6.01	19.31	6.75	18.73	0.33	2.86	7.93	0.59	0.74	0.32

order of $Y > B > G$, suggesting that these materials exhibit easier shape deformation than volumetric deformation and possess a high-stiffness characteristic. Additionally, we computed the Kleinman coefficient (ζ) to assess the given materials' resistance to bond bending and bond angle distortions, using equations specified elsewhere.[40] The Kleinman parameter (ζ), in the specified range of $0 \leq \zeta < 1$, is used to evaluate the contribution of both stretching and bending of the bonds within the material. For the titled materials, a smaller Kleinman parameter (ζ) indicates more resistance to bond bending and bond angle distortions.

To explore the fragility aspect of the given materials, parameters such as Cauchy's pressure, Pugh's ratio, and Poisson's ratio[40–42] have been computed and presented in Table 3. Cauchy's pressure, represented by the difference (C_{12}–C_{44}), functions as an indicator reflecting the ductile or malleable nature of a material. A positive sign denotes ductile character, while a negative sign signifies malleability. Pugh's ratio (B/G), with a critical threshold of 1.75, classifies materials as either ductile (above the threshold) or malleable (below the threshold). Poisson's ratio serves (ν) as an indicator of a material's brittleness or ductility. When Poisson's ratio exceeds 0.26, the material is considered ductile, whereas a ratio below 0.26 signifies malleability. The computed values of these parameters, as outlined in Table 3, collectively indicate the ductile characteristics of the provided materials.

In the field of crystallophysics, the importance of anisotropy metrics such as Zener anisotropic metric (A_Z) and universal anisotropic factor (A_U) is widely recognized. Hence, we computed these parameters to assess the anisotropy within our systems, utilizing the equations[43,44] $A_Z = \frac{2C_{44}}{C_{11} - C_{12}}$ and $A_U = 5\frac{G_V}{G_R} - 5$. The computed results, presented in Table 3, unequivocally indicate that the investigated compounds exhibit significant anisotropy in their nature, as both A_Z and A_U deviate from unity (where A_Z and A_U = 1 signifies isotropic materials).

Table 4 Computed values of transverse (V_t in m s^{-1}), longitudinal (V_l in m s^{-1}) and average sound velocity (V_{av} in m s^{-1}), Frantsevich's ratio (G/B) (unitless), machinability factor (μ_m) (unitless), Vickers hardness (H_V) (unitless), and melting temperature (T_m in K) for K_2GeMnX_6 perovskites

Parameter	V_t	V_l	V_{av}	G/B	μ_m	$(H_V)_{Teter}$	$(H_V)_{Tian}$	$T_m \pm 300$
$K_2GeMnCl_6$	2565	4545	2978	0.55	3.02	2.48	4.53	890
$K_2GeMnBr_6$	1609	3255	2395	0.36	4.04	1.36	3.67	824
K_2GeMnI_6	1305	2672	2043	0.34	3.21	1.02	0.86	730

A key objective in performing mechanical constant computations is to glean insights into the average sound velocity (V_{av}), estimated through transverse and longitudinal velocities (V_t and V_l). These velocities are calculated using equations[40]

$$V_t = \sqrt{\frac{G}{\rho}} \text{ and } V_l = B = \sqrt{\frac{(3B+4G)}{3\rho}}; \quad V_{av} = \left(\frac{1}{3}\right)^{\frac{1}{3}} \left(\frac{2}{v_s{}^3} + \frac{1}{v_l{}^3}\right)^{-\frac{1}{3}},$$

where ρ represents the density. The observed decline in V_{av} from Cl to I, as evident in Table 4, could be associated with the increasing density of these compounds (I > Br > Cl). Furthermore, various critical characteristics essential for real-world applications in thermoelectric materials, such as Vickers hardness (H_V), machinability factor (μ_m), Frantsevich's ratio (G/B), and melting temperature (T_m), are also computed using the following equations:[40,45–47]

$$(H_V)_{Teter} = 0.151\ G,\ (H_V)_{Tian} = 0.92(G/B)^{1.137}\ G^{0.708}$$

$$\mu_m = \frac{B}{C_{44}}$$

$$T_m\ (K) = [553\ (K) + (5.911)C_{11}]GPa \pm 300$$

All these parameters are compiled in Table 4. The computed Vickers hardness (H_V) values, obtained from two distinct estimations proposed by Teter *et al.*[45] and Tian *et al.*,[46] consistently yield positive values across all examined materials in both methods, indicating the high hardness of the given materials. The machinability factor (μ_m) underscores the suitable machinability level of the studied perovskites, characterized by reduced feed forces and mild lubricating properties. Furthermore, the estimated elevated melting temperature (T_m) coupled with a small G/B ratio suggests that these compounds hold promise as potential candidates for future thermoelectric materials, particularly for high-temperature applications.

3.5. Energy bands

The electronic structure of a material, elucidating the intricate arrangement and behaviour of electrons within its atomic or molecular framework, is pivotal for understanding its physical, chemical, and electronic properties. The electronic profile of the studied materials has been analyzed through spin-polarized band structure (BS) and density of states (DOS) evaluations. Utilizing both GGA and GGA+mBJ approximations, the band structures have been delineated, as depicted in Fig. 6(a–c). In the illustration, the band structure derived from GGA calculations indicates an unoccupied Fermi level in both spin

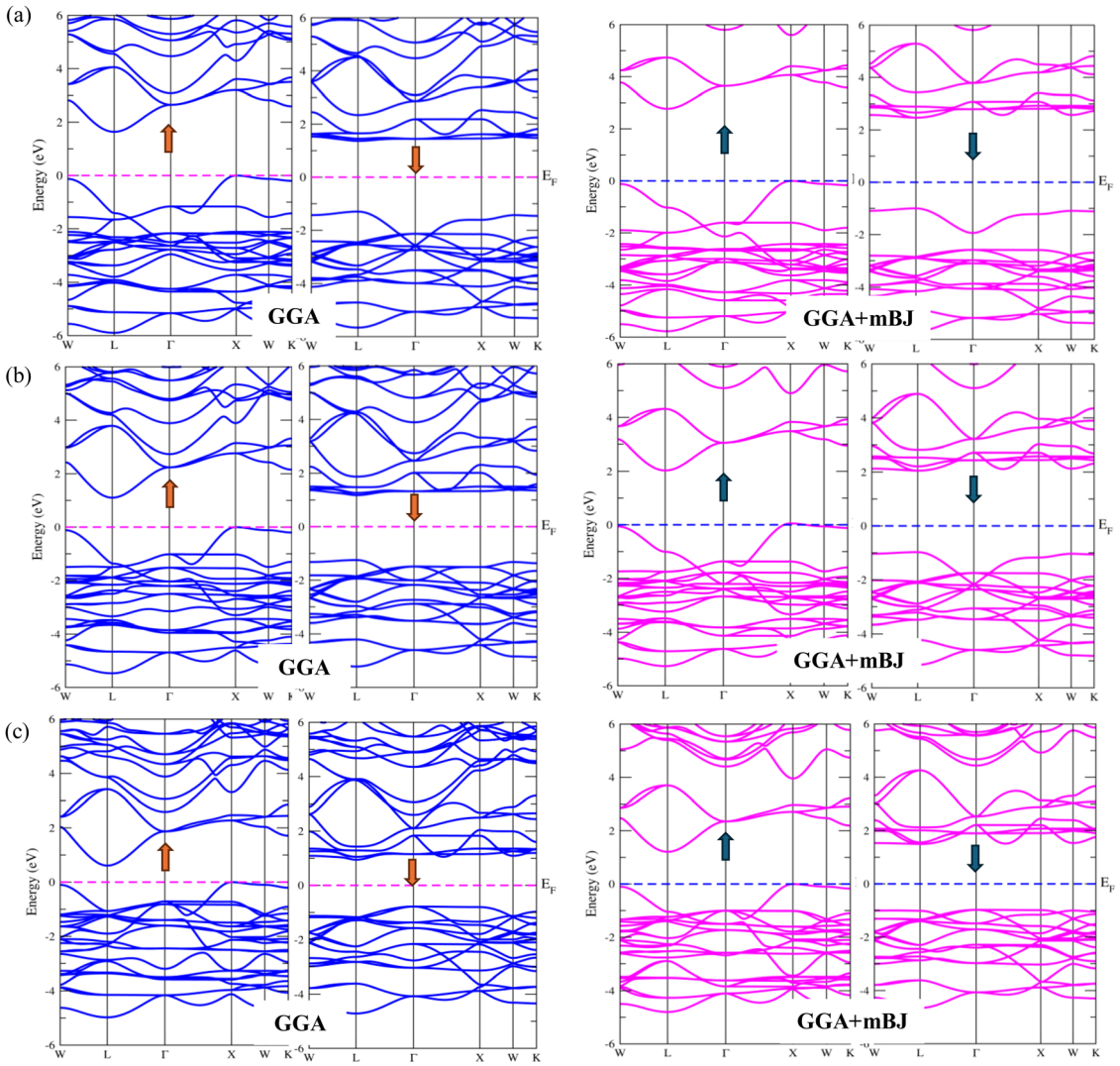

Fig. 6 DFT executed spin polarised band structure of (a) $K_2GeMnCl_6$, (b) $K_2GeMnBr_6$, and (c) K_2GeMnI_6 halide perovskites calculated *via* GGA and GGA+mBJ approximations. The upward arrow represents the spin-up channel, while the downward arrow signifies the spin-down channel.

directions for K_2GeMnX_6 (X = Cl, Br, I) halide perovskites. In the up-spin direction of all three materials, the Fermi level tangentially touches the valence band maximum, while in the spin-down direction, the Fermi level remains unoccupied. Nevertheless, a band gap exists in both spin channels, confirming the ferromagnetic semiconducting behavior of these materials. The band gap, defined as the energy separation between the top of the valence band and the minimum of the conduction band (CB), is crucial in elucidating electron behavior within the system. The computed values of the band gap obtained *via* GGA and GGA+mBJ potential are provided in Table 5. Considering the potential underestimation of the band gap value by the GGA approximation due to correlated d-electrons of transition atoms, the integration of the mBJ potential with GGA provides consistent electronic profiles for K_2GeMnX_6 (X = Cl, Br, I) perovskites, accompanied by modified band gap values, as presented in Table 5. The computed band gap values exhibit favourable agreement with analogous findings reported in the existing literature.[18,20] A more in-depth examination of the energy bands indicates increased dispersion in electronic states for spin-up channels in both the valence and conduction bands, leading to a reduction in the effective mass of charge carriers. Conversely, spin-down states exhibit less dispersive electronic states, leading to relatively high effective mass. This variation in effective mass suggests promising prospects for

Table 5 Illustrated values of the band gap (eV) and spin-splitting gap (eV), determined *via* GGA and GGA+mBJ approximations, for K_2GeMnX_6 (X = Cl, Br, I) halide perovskites

Parameter	Band gap				Spin-splitting gap			
Approximation	GGA		GGA+mBJ		GGA		GGA+mBJ	
Spin channel	Up	down	Up	down	ΔE_{CBM}	ΔE_{VBM}	ΔE_{CBM}	ΔE_{VBM}
$K_2GeMnCl_6$	1.62	2.63	2.75	3.46	0.27	1.28	0.29	1.02
$K_2GeMnBr_6$	1.09	2.41	2.01	3.00	−0.08	1.24	−0.04	0.78
K_2GeMnI_6	0.61	1.71	1.21	2.45	−0.34	0.78	−0.32	0.98

these materials in transport dynamics. Additionally, we calculated the spin-splitting gap, which represents the energy difference between the valence band maximum (VBM) or the conduction band minimum (CBM) and the Fermi level for spin-up and spin-down channels. The computed values of the spin splitting gap, as presented in Table 5, exhibit favorable agreement with results published for analogous materials.[18] These findings emphasize notable spin splitting, indicating a promising route for these materials towards advancements in semiconductor spintronics.

3.5.1. Density of states and origin of the semiconducting gap. The electronic properties of materials can be further explained from density of states (DOS) and partial density of states (PDOS) as shown in Fig. 7. These DOS plots also confirm the semi-conducting nature of K_2GeMnX_6 (X = Br, I) aligning well with the band structure. The exhibition of semiconducting nature in these halide systems within the sophisticated scheme of mBJ matches exactly well with the neighbouring series of alloys reported in the literature.[18,20]

The elucidation of atomic contributions to band formation and peaks in the density of states (DOS) plot is achieved through the presentation of the atomic DOS plot, as depicted in Fig. 7. In the context of these double perovskites, the halogen atom predominantly contributes to the upper valence band, whereas the Mn-d states dominate the conduction band. Notably, the d-t_{2g}/d-e_g states, positioned in the vicinity of the Fermi level, play a pivotal role in shaping the overall electronic properties of the present systems. To further elucidate the origin of semiconducting behaviour within these materials, the crystal field splitting of degenerate states of transition element Mn^{+2} needs to be calibrated. In the structural arrangement of K_2GeMnX_6 (X = Cl, Br, I), the central Mn atom is enclosed by six neighbouring Cl/Br/I atoms, acting as ligands that approach the central metal atom. To simplify, we treat these ligands as symmetrically positioned along the Cartesian coordinate system's axis, creating a spherical field with the metal ion at the center. In a spherical field, all d-orbitals are energetically elevated compared to the free ion due to negative charge repulsions. However, not all d-orbitals are affected to the same extent. Orbitals lying under the axis ($d_{x^2-y^2}$ and d_{z^2}) experience stronger repulsion than those with lobes directed between the axes (d_{xy}, d_{yz}, d_{zx}). Consequently, the d-orbitals split into two sets: d-t_{2g} (doubly degenerate) and d-e_g (triply degenerate). The extent of separation between d-t_{2g} and d-e_g states in an octahedral complex is denoted by Δ, where Δ signifies the octahedral splitting. The electronic occupation within these orbital sets involves six electrons (3↑, 3↓) for d-t_{2g} and 4 electrons (2↑, 2↓) for d-e_g, adhering to the maximum capacity of 10 electrons in d-orbitals. The electron filling, determining whether a high spin or low spin state is formed, depends on crystal field splitting and the interaction of weak or strong ligands with the central metal atom. Given the weak field ligand Cl/Br/I surrounding the central metal, the splitting is small, and electron filling aligns with Hund's rule. For Mn^{+2} in the Mn-d orbital, the electron filling occurs as $3t_{2g}(\uparrow)$, $2e_g(\uparrow)$, $0t_{2g}(\downarrow)$, and $0e_g(\downarrow)$. The Mn-d-t_{2g} and Mn-d-e_g orbitals each have one electron for the spin-up state, and for the opposite spin-down state, these orbitals remain empty. Consequently, the energy levels of Mn-d-t_{2g} and Mn-d-e_g manifest their presence in the valence band, forming the valence band maximum (VBM), while the unoccupied states in the spin-down channel reside in the conduction band, forming the conduction band minimum (CBM). Additionally, the *p*-states of Cl/Br/I, which accept electrons from cations, are situated in the valence band. The collective portrayal of these energy states thus illustrates the semiconducting electronic structure of these alloys. This semiconducting ferromagnetic behaviour certifies their potential applications in optical devices such as light-emitting diodes (LEDs) and semiconductor lasers.

3.5.2. Magnetism and Curie temperature. Next, we delve into the magnetic properties of K_2GeMnX_6 alloys (X = Cl, Br, I), engaging various approximation schemes for evaluation. Specifically, we utilize the Hubbard correction to GGA (GGA+U) and the Tran–Blaha modified Becke–Johnson method (TB-mBJ) due to their advanced capabilities in addressing the intricate electronic states that influence magnetism within these systems. The selection of the Hubbard parameter (U) has been methodically made, with $U_{eff} = U - J$, where U represents the onsite Coulomb interaction, refined to a suitable value of 0.40 Ry. Additionally, the exchange term (J) was systematically varied from 0 to 0.05 eV for all alloys to elucidate the magnetic interaction among their constituents. The spin magnetic

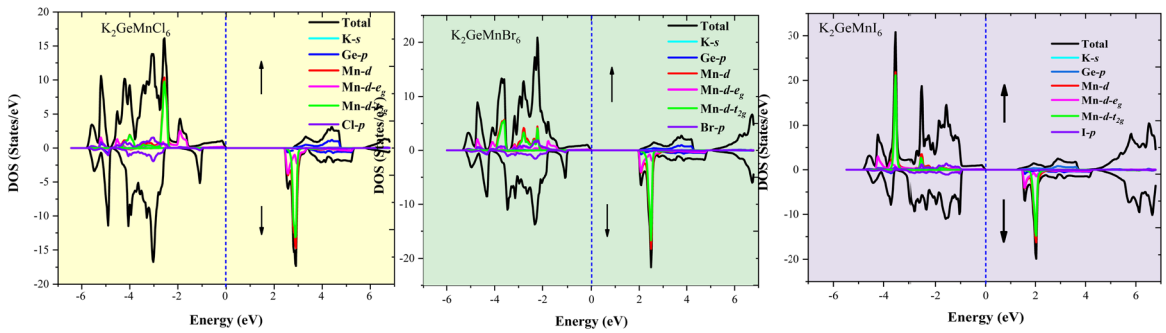

Fig. 7 Graphical representation of total density of states (TDOS) and projected density of states (PDOS) for K_2GeMnX_6 (X = Cl, Br, I) double perovskites determined *via* the GGA+mBJ approach.

Table 6 Calculated values of spin magnetic moments of mixed charge density for K_2GeMnX_6 (X = Cl, Br, I) compounds using GGA+U and TB-mBJ approximations

Material	Method	K (μ_B)	Ge (μ_B)	Mn (μ_B)	Cl/Br/I (μ_B)	Interstitial (μ_B)	Total (μ_B)
$K_2GeMnCl_6$	GGA+U	0.00	0.04	4.64	0.020	0.14	5.00
	GGA+mBJ	0.00	0.03	4.63	0.026	0.15	5.00
$K_2GeMnBr_6$	GGA+U	0.00	0.06	4.61	0.022	0.17	5.00
	GGA+mBJ	0.00	0.05	4.59	0.024	0.19	5.00
K_2GeMnI_6	GGA+U	0.00	0.07	4.52	0.019	0.23	5.00
	GGA+mBJ	0.00	0.05	4.50	0.022	0.22	5.00

moments, encompassing both total and partial moments, calculated using both GGA+U and TB-mBJ approaches for the K_2GeMnX_6 compounds, are summarized in Table 6. The outcomes from both GGA+U and GGA+mBJ approximations demonstrate consistency across the employed functionals. Notably, both the methods yield a total magnetism of $5\mu_B$ for each compound. The rationale behind these theoretical values is straightforward, rooted in the fact that the lattice structures of K_2GeMnX_6 foster five unpaired spins, resulting in a favourable magnetism of $5\mu_B$ for each compound. Considering the electronic configuration of the Mn-3d state as $4s^2\ 3d^5$, crystal field theory illustrates the splitting of the Mn-3d state into d-t_{2g} and d-e_g. Adherence to Hund's criterion reinforces the validity of the electron configuration as $3t_{2g}(\uparrow)$, $2e_g(\uparrow)$, $0t_{2g}(\downarrow)$ and $0e_g(\downarrow)$ and each half unpaired spin contributes $1\mu_B$ towards the lattice structure. Here, the aggregate tally of unpaired electron spins amounts to 5, thereby yielding a magnetic moment of $5\mu_B$. As a result, these alloys distinctly manifest a magnetic character, each attaining a value of $5\mu_B$, affirming their identity as ferromagnetic semiconductors. The integral magnetism is indicative of 100% spin-polarization at the Fermi level, rendering these alloys conducive to generating spin-polarized currents. The significant magnetism inherent in their lattice structure positions them favourably for application in spintronics and diverse technological advancements reliant on spin-based principles.

Furthermore, we determined the Curie temperature (T_C), which indicates the temperature at which a ferromagnetic or ferrimagnetic substance loses its permanent magnetization. Herein, we theoretically estimated the Curie temperature using the mean-field approximation (MFT) based on the Heisenberg model. In this approach, the Curie temperature for magnetic systems is calculated as[18,40] $T_C = \frac{2\Delta E}{3xK_B}$, where ΔE is a fundamental parameter in the Heisenberg model of the mean-field approximation and k_B is the Boltzmann constant. The projected Curie temperatures for the compounds $K_2GeMnCl_6$, $K_2GeMnBr_6$, and K_2GeMnI_6 are estimated to be 710 K, 650 K, and 570 K, respectively. Notably, these values significantly surpass those typically observed in double perovskite oxides. To elucidate the exceptionally high Curie temperatures manifested by the halide double perovskites in comparison to their oxide counterparts, a comparative analysis is conducted between the present halide perovskite $K_2GeMnCl_6$ and the double perovskite Bi_2CrOsO_6. This comparative exploration aims to uncover the underlying factors contributing to the elevated Curie temperature (T_C) in these halide perovskite systems. Exchange parameters are determined by their coupling styles. Given that the distance between two adjacent transition metal ions exceeds 7.0 Å, any direct coupling between them is expected to be negligible. Instead, the primary contributor to the ultrahigh T_C is identified as the indirect exchange coupling facilitated through GeX_6 groups situated between the two transition metal ions. In Fig. 7, a pronounced coupling between Mn 3d and Cl/Br/I 3p/4p/5p orbitals is evident. Consequently, the indirect coupling is elucidated as a 90° quasi-super exchange model between Mn 3d and $GeBr_6$ σ_{s-p^*} orbitals. In contrast, the coupling model for double perovskite oxides (DPOs) involves an 180° super exchange mechanism, characterized by Cr(d)–O(p)–Os(d) interactions. Notably, the application of a 90° super exchange interaction is deemed more suitable for ferromagnetic interactions compared to the 180° super exchange model, aligning with Pauli's exclusion principle.

For a compound exhibiting ferromagnetic interaction, the Curie–Weiss law predicts a positive value for the Curie–Weiss constant, denoted as T_θ. Conversely, a negative T_θ value suggests the prevalence of antiferromagnetic interactions among transition metals. The calculation of magnetic susceptibility is employed to identify the magnetic ground state. The magnetic susceptibility curves in Fig. 8 distinctly reveal that the reciprocal of the susceptibility curve yields positive values for the Curie–Weiss constant (T_θ) at approximately 101 K, 100 K and 90 K for $K_2GeMnCl_6$, $K_2GeMnBr_6$ and K_2GeMnI_6, respectively. For $T_\theta > 0$, signifying the presence of ferromagnetic interactions, the explanation provided by the Curie–Weiss law[40] holds true. Consequently, the stable ground state for K_2GeMnX_6 (X = Cl, Br, I) compounds is identified as the ferromagnetic phase.

3.6. Electron charge density distribution

The analysis of electronic charge density provides a unique perspective for understanding the chemical stability of K_2GeMnX_6 (X = Cl, Br, I) perovskites. In this context, we present the spin-polarized charge densities along the (111) plane, as depicted in Fig. 9. Notably, maximum electron cloud density is observed at the atomic positions. Our investigation aims to estimate and elucidate the bonding characteristics among distinct atoms interacting within their lattice structures. In accordance with Pauling's theory, a chemical bond is deemed to exist between two atoms when the bonding force is

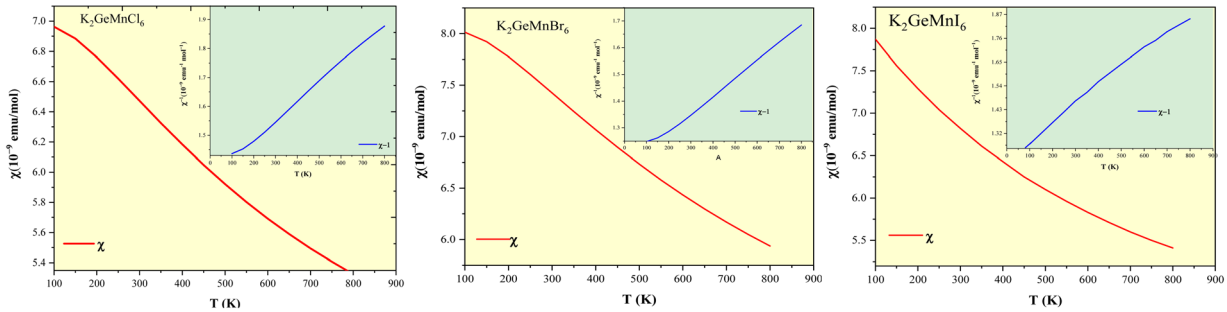

Fig. 8 Variation of magnetic susceptibility (χ) and its reciprocal (χ^{-1}) against temperature for K_2GeMnX_6 (X = Cl, Br, I) halide perovskites.

exceptionally strong. Furthermore, electronegative atoms are those that accept electrons, while electropositive atoms are characterized by electron donation. This characterization is applicable to all the systems under consideration. The analysis discerns the presence of ionic bonding between K and X(Cl/Br/I) atoms, where the electron cloud surrounding K and X(Cl/Br/I) atoms is notably spherical. On the contrary, the bonding between Ge/Mn and X (Cl/Br/I) atoms demonstrates a purely covalent nature. This is evidenced by the presence of dumbbell-shaped electron clouds along Ge/Mn-X(Cl/Br/I) bonds, indicating the sharing of charge between Ge/Mn and X(Cl/Br/I) atoms. The overlapping charge contours signify orbital hybridization between Ge/Mn and Cl/Br/I, also confirmed by the partial density of states (PDOS) distribution, revealing Mn-3d-X-p hybridization. The overall depiction reveals the presence of polar covalent bonding, a combination of covalent and ionic bonding intrinsic to these compounds.

3.7. Optical and dielectric properties

The assessment of a semiconductor's optical properties often entails the determination of band gaps and the complex dielectric function, denoted as $\varepsilon(\omega)$. This function comprises of two components, $\varepsilon(\omega) = \varepsilon_1(\omega) + i\varepsilon_2(\omega)$, where $\varepsilon_1(\omega)$ describes the scattering behavior of the material. Conversely, the imaginary part $\varepsilon_2(\omega)$ exhibits a direct correlation with the material's band structure, reflecting its absorptive behavior and offering valuable insights into material selection for solar cell technology applications. The interplay between the dielectric constant components adheres to the principles outlined by the Kramers–Kronig relationships.[34] Given the ferromagnetic semiconducting behavior observed in both spin channels of the materials under investigation, we assessed their optical properties by merging contributions from both spin channels to present a comprehensive optical response. Herein, we computed essential optical parameters for K_2GeMnX_6 halides as functions of photon energy, encompassing the dielectric function, refractive index, extinction coefficient, absorption coefficient, and optical conductivity, as illustrated in Fig. 10(a–f). This investigation aims to understand their capability to absorb visible light and their interaction with externally applied electromagnetic fields.

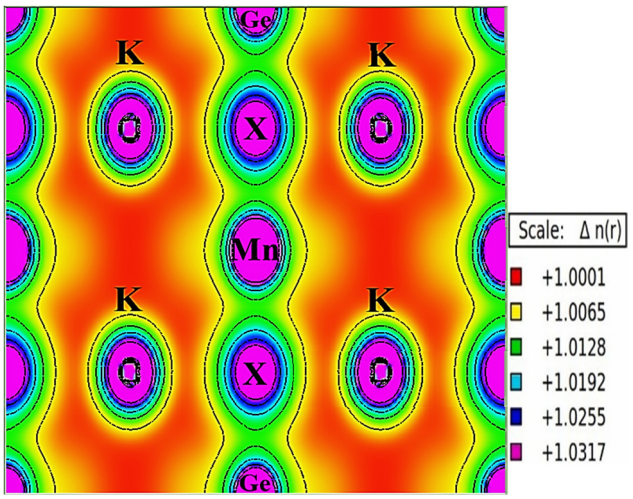

Fig. 9 Design of electronic charge density of K_2GeMnX_6 (X = Cl, Br, I) halide perovskites.

We begin by examining the graphical variations in the real component of the dielectric function ($\varepsilon_1(\omega)$) concerning photon energy, as depicted in Fig. 10(a). It is observed that the dielectric constant exhibits a systematic increase with changing halide ions, progressing from Cl to I. Notably, K_2GeMnI_6 exhibits higher static dielectric constants due to its smaller band gap, enabling reduced energy barriers for charge carrier movement. This facilitates carrier screening from charged defects within the crystal lattice, resulting in elevated dielectric constants. A high static dielectric constant facilitates the screening of carriers from charged defects within a crystal, thereby reducing carrier trapping and scattering. This reduction in scattering can result in semiconductors achieving longer carrier diffusion lengths and improved mobility lifetime outcomes. As photon energy increases, the spectra of all compounds show an upward trend. In the visible spectrum, K_2GeMnI_6 manifests a peak dielectric constant of about 8.0 at approximately 2.2 eV, whereas $K_2GeMnCl_6$ and $K_2GeMnBr_6$ attain maximal values of 5.1 and 6.2, respectively, at around 3.5 eV and 3 eV. Subsequently, multiple peaks are observed at different photon energies. Furthermore, Fig. 10(a) illustrates that transitioning the halide from Cl to I in K_2GeMnX_6 shifts the curves towards the visible energy range with increased amplitude. Consequently, there is an augmentation in the ε_1 spectra, accompanied by a shift of peaks towards lower energies. The imaginary part of the dielectric function signifies the

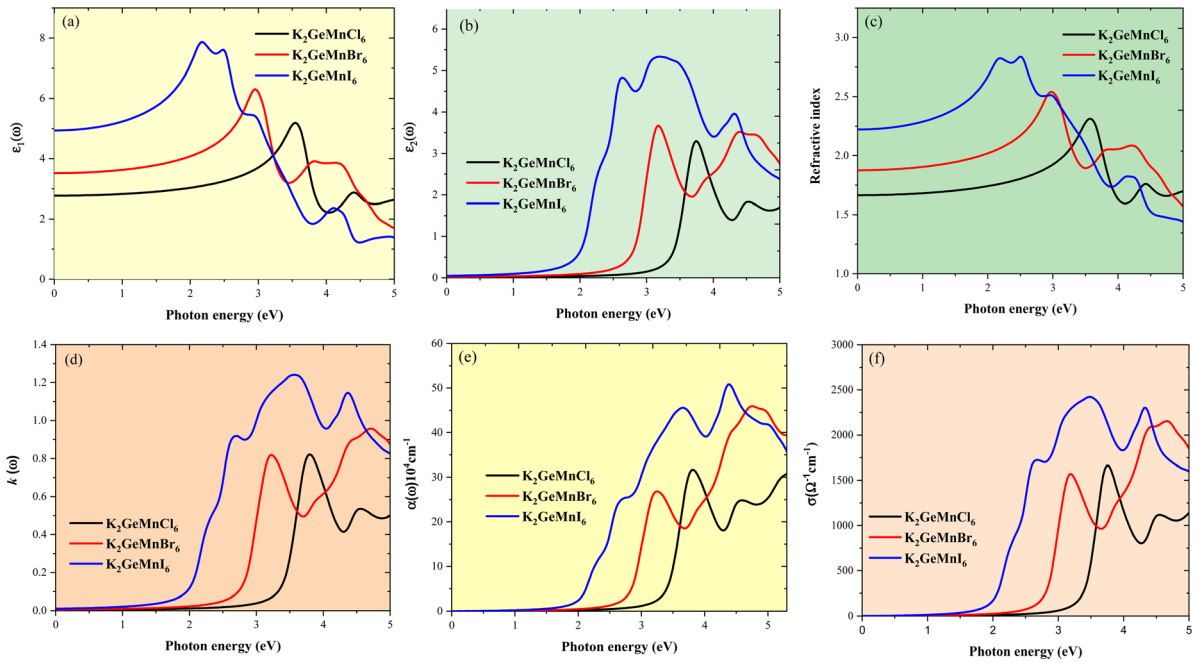

Fig. 10 The computed (a) real part of dielectric ($\varepsilon_1(\omega)$), (b) imaginary part of dielectric ($\varepsilon_2(\omega)$), (c) refractive index ($n(\omega)$), (d) extinction coefficient ($k(\omega)$), (e) absorption coefficient ($\alpha(\omega)$) and (f) photoconductivity (σ) for K_2GeMnX_6 (X = Cl, Br, I) halide perovskites.

absorption or dissipation of light as it traverses through a material. In Fig. 10(b), the calculated imaginary dielectric spectra ($\varepsilon_2(\omega)$ of K_2GeMnX_6 are presented. These spectra exhibit various peaks with varying amplitudes, resulting from potential electronic transitions from the valence band to the conduction band. Within the visible light range, the first peak in the $\varepsilon_2(\omega)$ curve corresponds to optical transitions between the highest valence bands of X (Cl-3p, Br-4p, or I-5p) and the lowest conduction bands of Mn-3d states. Additionally, a second significant peak in the energy range of 3.8 to 5.7 eV arises from optical transitions between the highest valence bands of Cl-3p, Br-4p, or I-5p orbitals and the conduction bands of Ge-p orbitals, situated far from the Fermi level. For $K_2GeMnCl_6$, $K_2GeMnBr_6$, and K_2GeMnI_6, their respective maximum values of 3.4, 3.6, and 5.4 occur at approximately 3.8 eV, 3.3 eV, and 3.3 eV. Notably, K_2GeMnI_6 exhibits a significant initial peak (4.9) at 2.6 eV, indicating its robust response to visible light. The inclusive analysis highlights the potential of inorganic K_2GeMnX_6 perovskites as promising alternatives to organolead halide perovskites.

Next, we examine the graphical fluctuations of the refractive index, $n(\omega)$, and the extinction coefficient, $k(\omega)$, with respect to photon energy, as illustrated in Fig. 10(c) and (d) respectively. The refractive index quantifies the speed of light propagation through a material, while the extinction coefficient describes the attenuation of light as it traverses the medium due to absorption and scattering per unit distance. The static refractive index values, $n(0)$, are determined to be 1.6, 1.8, and 2.2 for $K_2GeMnCl_6$, $K_2GeMnBr_6$, and K_2GeMnI_6, respectively. Beyond the zero-frequency limit, the refractive index reaches its maximum value of 2.3 at approximately 3.5 eV for $K_2GeMnCl_6$, 2.55 at 3.0 eV for $K_2GeMnBr_6$ and 2.8 at 2.2 eV for K_2GeMnI_6, followed by a consistent decrease with increasing photon energy. This decline in the refractive index is likely attributed to the optical dispersion behavior of these materials. Conversely, the extinction coefficient, $k(\omega)$, exhibits a profile resembling the imaginary part of the dielectric constant. Notably, significant absorption is observed in $k(\omega)$, featuring peaks situated around 2.5 eV and 3.5 eV for K_2GeMnI_6, and approximately 3.7 eV and 3.2 eV for $K_2GeMnCl_6$ and $K_2GeMnBr_6$.

The absorption coefficient ($\alpha(\omega)$) serves as a crucial parameter for characterizing the photovoltaic properties of semiconductors, governing the extent to which light penetrates a medium and indicating the semiconductor's capability to capture light effectively. Fig. 10(e) illustrates the computed absorption spectra of K_2GeMnX_6 compounds against photon energy, showcasing prominent peaks spanning both the visible and ultraviolet spectral regions. It is evident that the absorption coefficients surpass 10^4 cm^{-1} for all compounds, with $K_2GeMnBr_6$ and K_2GeMnI_6 demonstrating optimal light absorption characteristics in the visible light range, while $K_2GeMnCl_6$ exhibits optimum absorption properties in the ultraviolet region. Specifically, in the energy range of 0–5.5 eV, K_2GeMnI_6 and $K_2GeMnBr_6$ demonstrate maximum light absorption of 50×10^4 cm^{-1} and 45×10^4 cm^{-1} at a photon energy of 4.5 eV and 4.8 eV, whereas $K_2GeMnCl_6$ exhibits an optimal absorption value of 33×10^4 cm^{-1} at approximately 5.3 eV. Peaks observed away from zero energy indicate the absence of energy states at the Fermi level, confirming the semiconducting nature of these materials. The significant absorption coefficients in the visible and ultraviolet spectrum primarily stem from the abundant and localized

density of states near the Fermi level, coupled with the materials' low band gap. Moreover, as halogen anions increase in size, the absorption spectrum shifts towards the redshift direction, consistent with the band gap trend discussed above. A solar absorber characterized by a high absorption coefficient is highly advantageous for optimizing cell performance due to the minimized travel distance required for photogenerated carriers prior to recombination. This effectively diminishes non-radiative recombination processes, consequently leading to a significant enhancement in the open circuit voltage of photovoltaic cells. The utilization of thin absorber layers, facilitated by the high absorption coefficients, contributes to a reduction in the fabrication costs associated with solar cells. The optical conductivity (σ) of these halide perovskites exhibits a similar variation as the optical absorption, as depicted in Fig. 10(f). This correlation arises from the fact that absorbed photons generate conduction carriers, thereby increasing conductivity. From Fig. 10(f), it can be inferred that these perovskites display high optical conductivity in the low-energy region. Specifically, K_2GeMnI_6 exhibits the highest magnitude of conductivity spectra, while the remaining compounds show slightly lower values, suggesting superior optical conductivity for K_2GeMnI_6 compared to the others. The elevated optical conductivity values further underscore the potential of these materials for photovoltaic applications. To conclude, Ge-based halide perovskites demonstrate enhanced optical characteristics when compared to their Pb and Sn counterparts, indicating encouraging directions for further experimental exploration.

3.8. Thermoelectric coefficients

The thermoelectric effect refers to the phenomenon where a temperature gradient applied across a material results in the generation of an electric voltage or current. This effect is utilized in thermoelectric devices for various applications, including power generation and temperature regulation. The key focus in this process is the figure of merit (zT), which quantifies the efficiency of the material in terms of interdependent thermoelectric parameters. Specifically, zT is determined from the association between the Seebeck coefficient (S), electrical conductivity (σ), thermal conductivity (κ), and temperature (T) according to the equation $zT = \frac{S^2\sigma}{\kappa}T$. This relationship highlights the importance of minimizing thermal conductivity (κ) while maximizing the square of the Seebeck coefficient (S) and electrical conductivity (σ) to achieve high output from a thermoelectric device. All these parameters have been determined using the Boltzmann transport theory within the rigid band approximation and constant relaxation time (τ) approximation, implemented through the BoltzTraP code.[26] The electron relaxation time (τ), a crucial parameter in evaluating thermoelectric properties, represents the average duration between successive electron scattering events. The approximation assumes limited energy dependence of thermoelectric parameters at the scale of thermal agitation (k_{BT}).[48] As long as the scattering time changes gradually with energy, thermoelectric coefficients like electronic thermal conductivity (κ_e/τ), electrical conductivity (σ/τ), and figure of merit $\left(\frac{S^2\sigma/\tau}{\kappa_e + \kappa_l}T\right)$ can be conveniently expressed in terms of τ.

In the course of this investigation, we thoroughly examined the impact of thermoelectric coefficients on both temperature variations and chemical potential dependency, as illustrated in Fig. 11(a–e) and 12 (a–c) The anticipated ferromagnetic behavior of the investigated compounds prompts an exploration

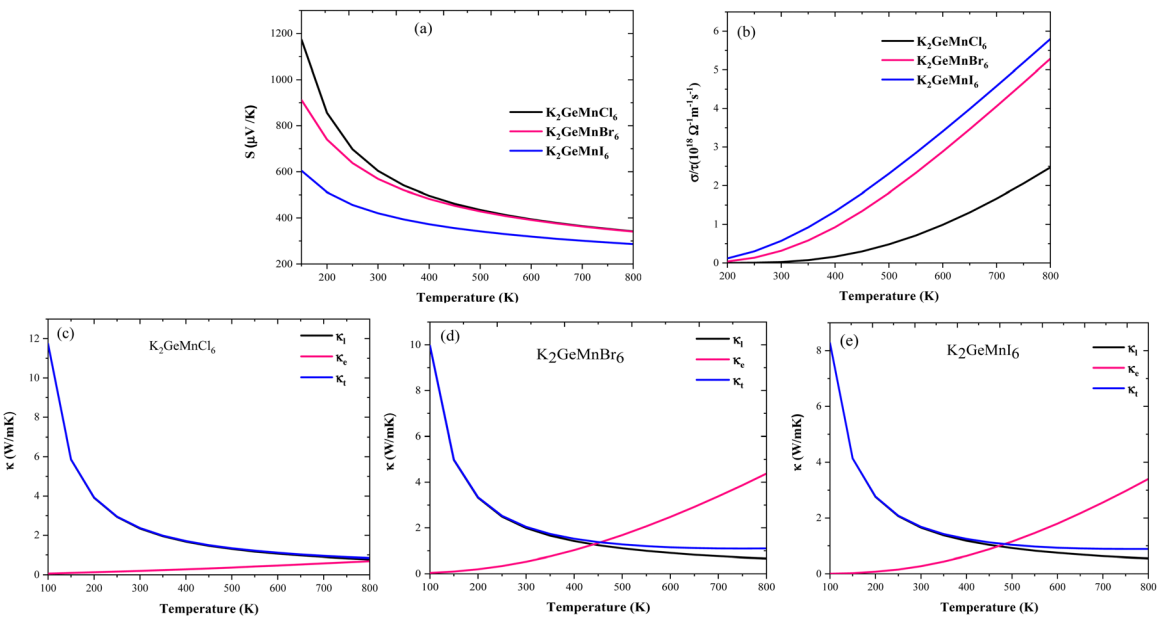

Fig. 11 Temperature variations for (a) Seebeck coefficient, (b) electrical conductivity, and (c)–(e) lattice, electronic and total thermal conductivity of K_2GeMnX_6 halide perovskites.

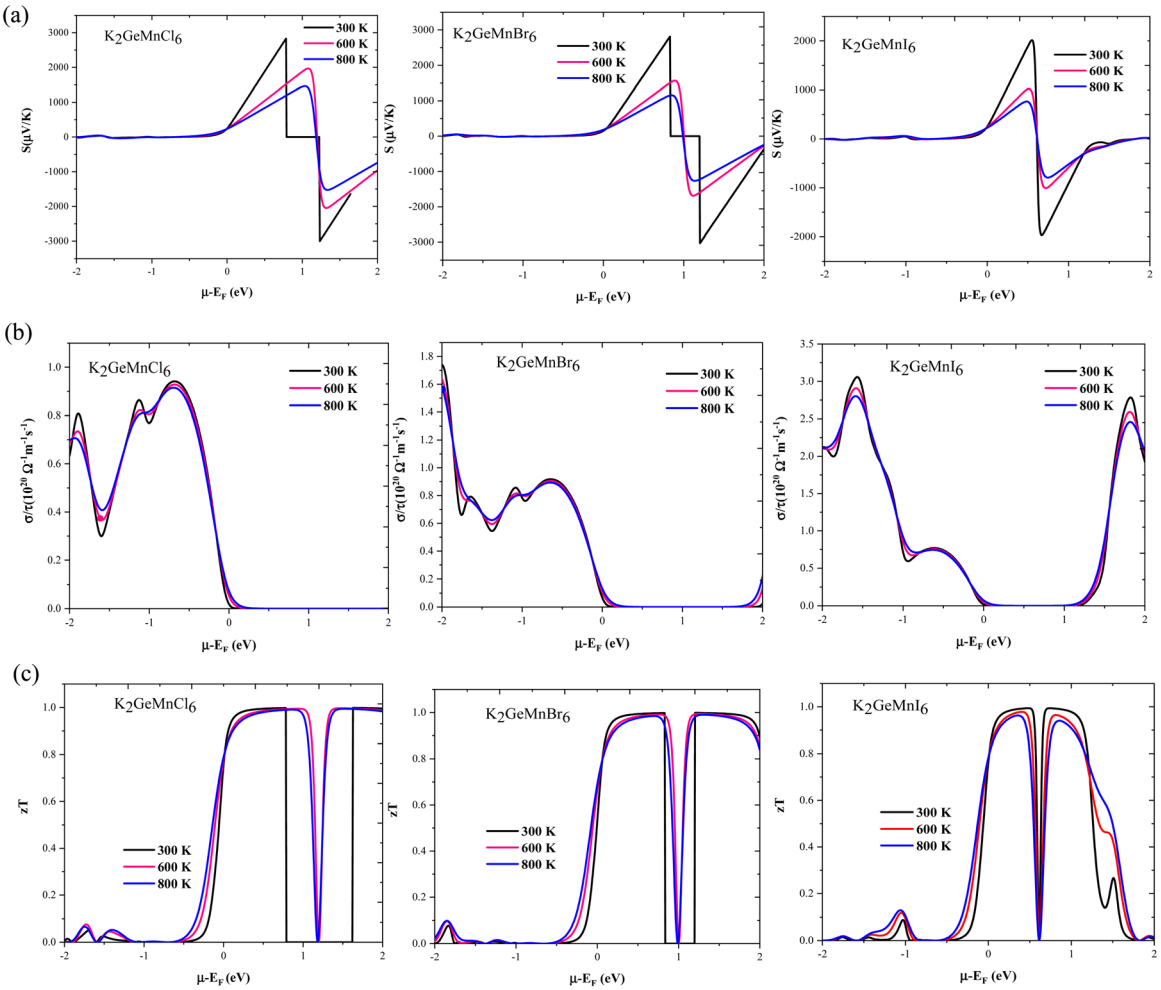

Fig. 12 Thermoelectric plots of (a) Seebeck coefficient (S), (b) electrical conductivity (σ/t), and (c) figure of merit (zT) against chemical potential at different temperatures (300 K, 600 K, 800 K) for K_2GeMnX_6 (X = Cl, Br, I) halide perovskites.

into the influence of magnetism on thermoelectric parameters. To discern this effect, we employed the two-current model,[40] a theoretical framework tailored for analysing the interplay between magnetism and thermoelectric properties, particularly prevalent in ferromagnetic materials. In this model, the electronic transport is delineated separately for spin-up (↑) and spin-down (↓) electrons, acknowledging their distinct contributions owing to magnetization. Within ferromagnetic materials, magnetization induces spin-dependent electronic transport phenomena, where spin-up and spin-down electrons encounter disparate scattering mechanisms and mobility due to interactions with local magnetic moments. Consequently, quantities such as electrical conductivity (σ), electronic thermal conductivity (κ_e), and Seebeck coefficient (S) become spin-dependent variables, denoted as $\sigma(\uparrow)$, $\sigma(\downarrow)$, $\kappa_e(\uparrow)$, $\kappa_e(\downarrow)$, $S(\uparrow)$, and $S(\downarrow)$ respectively. Through the application of the two-current model, we computed the total electrical conductivity ($\sigma = \sigma(\uparrow) + \sigma(\downarrow)$), total electronic thermal conductivity ($\kappa_e = \kappa_e(\uparrow) + \kappa_e(\downarrow)$), and total Seebeck coefficient $\left(S = \frac{S(\uparrow)\sigma(\uparrow) + S(\downarrow)\sigma(\downarrow)}{\sigma(\uparrow)\sigma(\downarrow)}\right)$. Here, $S(\uparrow)$, $S(\downarrow)$, $\sigma(\uparrow)$, and $\sigma(\downarrow)$ represent the Seebeck coefficient and electrical conductivity for spin-up and spin-down directions, respectively.

The subsequent detailed analysis of thermoelectric coefficients against temperature variations (200–800 K) and chemical potential dependency (−2 to 2 eV) is discussed below.

Seebeck coefficient. Thermoelectric materials exhibit the capacity to generate an electric voltage in response to a temperature gradient (ΔT). The effectiveness of this voltage generation is quantified by the Seebeck coefficient (S), expressed as $\Delta V = S\Delta T$.[49] The key determinants influencing the S-value in any thermoelectric material encompass carrier concentration and the scattering rate. In our analysis, we have examined the variation of the total Seebeck coefficient with temperature, as illustrated in Fig. 11(a). Notably, it is evident that the total S-value decreases with an increase in temperature. Specifically, the total Seebeck coefficient (S) exhibits a decline from high values of 1180 μV K^{-1}, 900 μV K^{-1}, and 600 μV K^{-1} at 150 K to 400 μV K^{-1}, 380 μV K^{-1}, and 250 μV K^{-1} at 800 K for $K_2GeMnCl_6$, $K_2GeMnBr_6$, and K_2GeMnI_6, respectively. To comprehend this behaviour, it is imperative to explore the dependency of the Seebeck coefficient on carrier concentration 'n',

expressed by the relation[40] $S = \frac{8\pi^2 k_B^2}{3e\hbar^2} m^* T \left(\frac{\pi}{3n}\right)^{2/3}$. Semiconductors behave as insulators at absolute zero (T = 0 K) due to the absence of current carriers, resulting in the expectation of an infinitely large S at absolute zero temperature. However, as the temperature rises, electrons acquire sufficient thermal energy to transition from the valence band to the conduction band, generating electron–hole pairs and consequently diminishing the magnitude of the Seebeck coefficient, as evident in Fig. 11(a).

In addition to temperature, we also scrutinized the impact of chemical potential ($-2 \leq \mu \geq 2$) on the total Seebeck coefficient at different temperatures (300 K, 600 K, 800 K), as illustrated in Fig. 12(a). The polarity of the Seebeck coefficient serves as an indicator of the type of charge carriers, with a positive sign denoting p-type carriers and a negative sign indicating n-type charge carriers. The magnitude of the Seebeck coefficient is intricately linked to the behaviour of energy levels in proximity to the Fermi level. Across the entire range of chemical potential (−2 to 2) eV, the Seebeck coefficient exhibits distinct peaks and valleys on either side of the Fermi level (set at zero). Particularly, prominent peaks manifest in the energy range of 0.5–2 eV for all three materials, where electronic states are either negligible or very limited, resulting in lower carrier concentration and pronounced peaks in this region. Preceding and succeeding this range, the presence of electronic states is evident, which subsequently diminishes the peaks almost to zero. At room temperature, the maximum Seebeck coefficients are ±2900 μV K^{-1} for $K_2GeMnCl_6$, ±2600 μV K^{-1} for $K_2GeMnBr_6$, and ±2000 μV K^{-1} for K_2GeNiI_6. These values are notably high, with $K_2GeMnCl_6$ exhibiting a relatively high Seebeck coefficient, attributed to its larger band gap. The elevated Seebeck coefficient values in these materials can be ascribed to their semiconducting behavior observed in both spin channels. To further elucidate the mechanism behind the high Seebeck coefficient of these compounds, we plotted the Seebeck coefficient alongside the volumetric density of states (DOS) and carrier concentration for $K_2GeMnCl_6$ in both spin channels, as depicted in Fig. 13. While a similar behavior is observed in other compounds, their data are omitted here for brevity. The Seebeck coefficient displays peaks in the energy range of 0–1 eV in the spin-up channel and −1 to 0 eV in the spin-down channel, coinciding with regions where the volumetric DOS is either low or negligible. This leads to low carrier concentration predominantly of p-type, facilitating a higher Seebeck coefficient by promoting increased carrier mobility, optimizing energy levels, and minimizing carrier scattering and Auger recombination. Furthermore, in semiconductors, the Seebeck coefficient is intricately linked to the electronic band structure near the Fermi level. At reduced carrier concentrations, the Fermi level tends to approach the band edges, leading to a pronounced gradient in the density of states. This phenomenon augments the Seebeck coefficient by enlarging the reservoir of available states accessible to charge carriers, thereby intensifying the thermoelectric response.

From Fig. 12(a), it is evident that at 800 K, the peak Seebeck coefficients experience a decrease to approximately ±1500 μV K^{-1} for $K_2GeMnCl_6$, ±1000 μV K^{-1} for $K_2GeMnBr_6$, and ±700 μV K^{-1} for K_2GeMnI_6. These results align precisely with the Mott relation, a fundamental expression capturing the dependence of the Seebeck coefficient on chemical potential and temperature, given as[50] $S = \frac{\pi^2 k_B^2 T}{3e}\left\{\frac{1dn(\varepsilon)}{nd\varepsilon} + \frac{1dn(\varepsilon)}{\mu d\varepsilon}\right\}_{\varepsilon=\mu}$. This equation elucidates that as both chemical potential (μ) and temperature (T) increase, the Seebeck coefficient experiences a decline. This behaviour can be attributed to the stimulation of both types of carriers, resulting in a bipolar effect. Nevertheless, the given compounds effectively avoid the bipolar effect as their band gaps exceed the critical threshold of 0.64 eV, below which the bipolar effect is typically observed. Therefore, the presence of a non-zero Seebeck coefficient (S) even at elevated temperatures suggests promising potential for

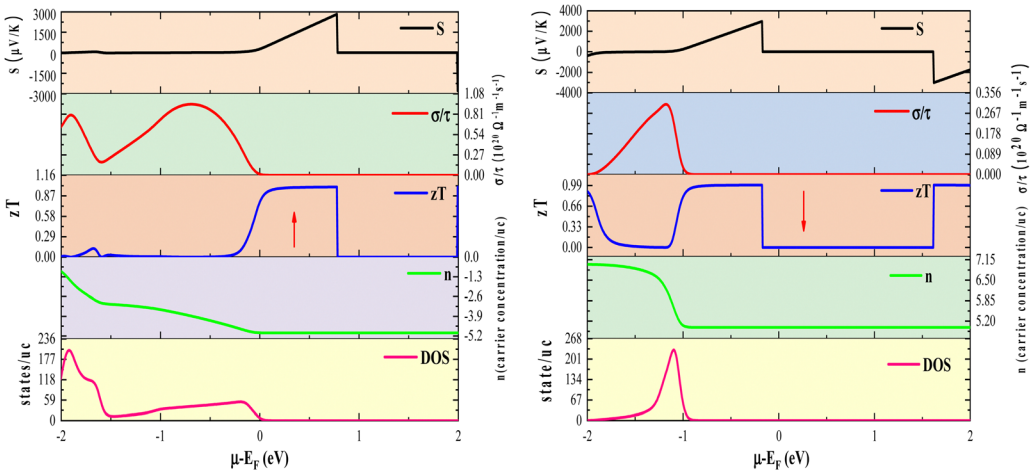

Fig. 13 Comparative variation in Seebeck coefficient (S), electrical conductivity (σ/t), figure of merit (zT), carrier concentration (n) and volumetric density of states (DOS) against chemical potential at 300 K, for the $K_2GeMnCl_6$ halide perovskite (the upward and downward arrows indicate spin-up and spin-down directions, respectively).

these materials in various applications such as thermoelectric generators, thermoelectric coolers, thermocouples, and temperature sensors.

Electrical conductivity. The temperature-dependent variation in electrical conductivity coefficient (σ/τ) is illustrated in Fig. 11(b). The electronic conductivity of the given K_2GeMnX_6 double perovskites demonstrates an increasing trend with temperature, indicative of a semiconducting nature. This rise in electrical conductivity suggests a decrease in resistance with an elevation in temperature. The electrical conductivity values initiate their ascent from 200 K for all the three compounds, reaching a maximum value of 2.7×10^{18} (Ω^{-1} m^{-1} s^{-1}) for $K_2GeMnCl_6$, 5.0×10^{18} (Ω^{-1} m^{-1} s^{-1}) for $K_2GeMnBr_6$ and 5.6×10^{18} (Ω^{-1} m^{-1} s^{-1}) for K_2GeMnI_6 at 800 K. The coefficient of electrical conductivity is directly proportional to the carrier concentration (n), as given by the equation $\sigma = ne\mu$, where μ represents mobility and 'e' is the electronic charge.[35] At absolute zero temperature, the energy states below the Fermi level are completely filled, rendering these double perovskites insulators. However, as the temperature increases, electrons gain thermal energy, transitioning to the conduction band (CB) and generating pairs of carriers (holes in the valence band and electrons in the conduction band). Consequently, with rising temperature, the carrier number increases, leading to an elevation in conductivity. The temperature at which carriers sharply increase depends on the band gap value, with a higher band gap requiring more energy to traverse the band gap region. The higher magnitude of electrical conductivity observed in K_2GeMnI_6 compared to $K_2GeMnBr_6$ and $K_2GeMnCl_6$ can be attributed to the smaller band gap value in the former compared to the latter two compounds.

In the context of the chemical potential dependency of total electronic conductivity, we have graphically represented the total electrical conductivity at different temperatures (300, 600, and 800), as illustrated in Fig. 12(b). The most prominent peaks occur around -2 to 0 eV for all the three materials. Notably, $K_2GeMnCl_6$ exhibits higher band gap values in both spin channels compared to K_2GeMnB_6 and K_2GeMnI_6, leading to conductivity peaks slightly offset from the Fermi level. However, the presence of energy states at the Fermi level in one spin state contributes to the overall conductivity peaks at the Fermi value, specifically originating from spin-up electrons. Nevertheless, peaks on both sides of zero chemical potential arise from contributions by both types of spin electrons. Upon comparison of Fig. 12(a) with Fig. 12(b), it becomes evident that the Seebeck coefficient manifests peaks coinciding with conductivity minima, while conductivity exhibits peaks where the Seebeck coefficient is low or negligible. This association arises from the direct dependence of conductivity on carrier concentration ('n'), while the Seebeck coefficient varies inversely with 'n'.[40] In order to deepen our comprehension of the relationship between electrical conductivity and chemical potential, we have constructed plots illustrating the total electrical conductivity (σ/τ), carrier concentration (n), and volumetric density of states (DOS) as functions of chemical potential at a temperature of 300 K. These plots specifically pertain to the compound $K_2GeMnCl_6$, as depicted in Fig. 13 (others are not shown for brevity). Corresponding to the pseudo gap in the band structure, carrier concentration sharply decreases, leading to peaks in the Seebeck coefficient. On the other side, conductivity demonstrates peaks at chemical potentials corresponding to densely populated bands.

Thermal conductivity. Thermal conductivity, denoting the ability of a material to conduct heat through charge carriers, plays a critical role in thermoelectric phenomena. For optimal thermoelectric performance, it is essential for materials to exhibit low thermal conductivity. This attribute enables the maintenance of a substantial temperature gradient across the material, crucial for generating a significant thermoelectric voltage. In solids, thermal conductivity arises from both electronic contributions and lattice vibrations, mediated by phonons. The temperature-dependent variations in electronic, lattice, and total thermal conductivity are graphically represented in Fig. 11(c, d and e). Electronic thermal conductivity follows a trend similar to electrical conductivity, increasing with temperature. As the BoltzTraP code exclusively considers the electronic component, Slack's equation[51] is employed to determine the lattice part, which is given by the equation[40,51] $\kappa_l = \frac{A\theta_D{}^3 V^{1/3} m}{\gamma^2 N^{2/3} T}$; here, each symbol carries its usual significance. The Slack model elucidates that lattice thermal conductivity is influenced by multiple factors, including the Debye temperature (θ_D), Gruneisen parameter (γ), temperature (T), volume (V), average molar mass per atom (m), and the number of atoms per unit cell (N). The parameter A is determined as[51] $A = \frac{2.43 \times 10^8}{1 - \frac{0.514}{\gamma} + \frac{0.228}{\gamma^2}}$. Lattice thermal conductivity (κ_l), inversely proportional to temperature, diminishes as temperature rises for all three materials, as depicted in Fig. 11(c, d and e). The thermodynamic parameters required to compute lattice thermal conductivity in Slack's equation exhibit modest temperature variations, with the magnitude primarily dependent on the number of atoms per unit cell. Notably, the presence of 10 atoms per unit cell, combined with intricate cage structures housing small atoms, results in a remarkably low lattice thermal conductivity at room temperature. This phenomenon can be attributed to heightened anharmonic phonon scattering due to the clustering of heavier elements, commonly referred to as the 'phonon rattling effect'.[52] Conversely, electronic thermal conductivity displays an upward trajectory with rising temperature. Higher temperatures amplify the thermal energy of carriers, consequently enhancing electronic thermal conductivity. At temperatures below 300 K, the lattice component of thermal conductivity prevails over the electronic contribution. However, with increasing temperature up to approximately 900 K, the lattice thermal conductivity of all the given materials exhibits a consistent decrease. Specifically, at 300 K, the computed lattice thermal conductivity values are 2.2 W mK^{-1}, 2.0 W mK^{-1}, and 1.7 W mK^{-1} for $K_2GeMnCl_6$, $K_2GeMnBr_6$, and K_2GeMnI_6, respectively. These modest κ_l values observed in these materials hint at a promising potential for enhanced thermoelectric

performance. Notably, at higher temperatures, the total thermal conductivity is predominantly influenced by the electronic component due to the reduced contribution from the lattice. This overall low heat-carrying capacity positions these double perovskites as promising candidates for efficient waste heat harvesting applications.

Figure of merit (zT). The figure of merit (zT) serves as a crucial metric for evaluating the suitability of materials in the fabrication of thermoelectric devices. This dimensionless parameter quantifies the maximum conversion efficiency achievable by a thermoelectric device. The graphical representation of the variation in zT against the chemical potential at different temperatures is presented in Fig. 12(c). The plot illustrates that the zT values for all the three materials reach peak values near unity, with these peaks occurring in close proximity to the Fermi level. Nevertheless, with the ascent in temperature, the peak values experience a decline owing to the dual impact of diminishing Seebeck coefficient and escalating thermal conductivity associated with elevated temperatures. Notably, the high zT values of 1.01, 1.00 and 0.99 at room temperature for $K_2GeMnCl_6$, $K_2GeMnBr_6$ and K_2GeMnI_6, respectively, can be attributed to the ultra-low thermal conductivity exhibited by these materials. These values exceed those of comparable materials documented in the literature.[19] The peaks in the thermoelectric figure of merit (zT) for all compounds are observed within the energy range of 0–1 eV, in close proximity to the Fermi level, indicating the significant potential of these double perovskites in renewable energy and thermoelectric device applications.

To elucidate the high thermoelectric figure of merit of these materials and explore avenues for further enhancing the achieved zT values, we conducted a comparative analysis of the graphical variations in density of states (DOS), carrier concentration (n), and figure of merit (zT) at 300 K for $K_2GeMnCl_6$ in both spin-up and spin-down channels, as shown in Fig. 13. Given the consistent behavior observed across all three materials, our examination focuses exclusively on the $K_2GeMnCl_6$ halide perovskite. Peaks in zT, as depicted in Fig. 13, are notably prominent within the energy range of -1 to 1 eV in both spin channels, attributable to diminishing electronic states in the DOS, resulting in a low carrier concentration, primarily of p-type, within this energy range. The reduction in the concentration of p-type carriers results in an increase in the Seebeck coefficient (S), as elucidated in the preceding discussion on the Seebeck coefficient. As a consequence, the heightened Seebeck coefficient enhances the thermoelectric voltage, thereby amplifying the zT value. However, it is pertinent to note that the attained zT values can be further enhanced through the application of strain effects or optimization of hole doping strategies, as demonstrated in previous studies.[53]

Conclusion

In summary, we have undertaken a comprehensive investigation into the structural, magneto-electronic, optical and transport properties of K_2GeMnX_6 (X = Cl, Br, I). The optimization of the structures ensures stability in the ferromagnetic phase, corroborated by positive Curie–Weiss constant values. Mechanical stability tests, tolerance factor evaluations, and negative enthalpy of formation further confirm the $Fm\bar{3}m$ cubic stability of these materials. Through the study of phonon dispersions, we have gained insights into the dynamic characteristics of these perovskites. The electronic properties, as delineated by the TB-mBJ functional scheme, affirm the ferromagnetic semiconducting nature of all three materials, characterized by a significant spin-splitting gap (0.28–1.02 eV), indicating their promising prospects for semiconductor spintronics. The magnetic character of K_2GeMnX_6 (X = Cl, Br, I) perovskites has been determined to exhibit an integer value of $5\mu_B$ each, validating their suitability for magneto-electronic device applications. Furthermore, the determined Curie temperatures, surpassing typical room temperature values, underscore their high-temperature phase stability. Analysis of electronic charge density plots suggests a polar covalent nature, indicating a mix of covalent and ionic bonding. Exploration of thermodynamic vibrational properties, including vibrational internal energy, vibrational Helmholtz free energy, vibrational entropy, and vibrational specific heat, indicates stability across varying temperature regimes. Moreover, the computed optical coefficients, including the dielectric constant, refractive index, and absorption coefficient, exhibit peak values within the visible spectrum. Notably, significant absorption coefficient values of 33×10^4 cm^{-1} for $K_2GeMnCl_6$, 45×10^4 cm^{-1} for $K_2GeMnBr_6$ and 50×10^4 cm^{-1} for K_2GeMnI_6 are observed across the visible and ultraviolet spectra, highlighting their promising potential for application in optoelectronic and solar cell technologies. Finally, the thermoelectric coefficients demonstrate a significant Seebeck coefficient coupled with reduced thermal conductivity, yielding high thermoelectric figure of merit (zT) values of 1.01, 1.00, and 0.99 for $K_2GeMnCl_6$, $K_2GeMnBr_6$ and K_2GeMnI_6, respectively. These findings highlight the potential applications of these perovskites in renewable energy technologies. The comprehensive analysis suggests that these materials hold promise for deployment in solid-state devices, green energy technologies, and various other technological domains. Despite the insightful findings, challenges persist in experimental observation. These encompass achieving uniformity in synthesis, accurately probing nanoscale structures, interpreting dynamic properties, precisely controlling doping levels, and ensuring reliable measurements of thermal and thermoelectric properties. Challenges specific to magnetism involve understanding magnetic interactions and achieving uniform magnetization, while optimizing the figure of merit (zT) requires balancing multiple thermoelectric parameters. Moreover, tackling experimental hurdles associated with comprehending and regulating optical properties, including the precise determination of dielectric constants and absorption coefficients, is paramount. Addressing these challenges is essential for unlocking the full potential of K_2GeMnX_6 perovskites in applications pertaining to spintronics, optoelectronics and thermoelectric devices.

Data availability

The data sets generated and thereafter analysed would be available from the corresponding author upon reasonable request.

Conflicts of interest

The authors declare no competing interest.

Acknowledgements

Mudasir Younis Sofi, a recipient of the Prime Minister Research Fellowship (PMRF) award (Letter No. 3302522), wishes to express sincere gratitude to the PMRF agency (Ministry of Education (MoE), Govt. of India) for the financial support.

References

1 T. Dietl, H. Ohno, F. Matsukura, J. Cibert and E. D. Ferrand, Zener model description of ferromagnetism in zinc blende magnetic semiconductors, *Science*, 2000, **287**, 1019.
2 Y. Huai, F. Albert, P. Nguyen, M. Pakala and T. Valet, Observation of spin-transfer switching in deep submicron-sized and low-resistance magnetic tunnel junctions, *Appl. Phys. Lett.*, 2004, **84**, 3118.
3 C. Chappert, A. Fert, F. Nguyen and V. Dau, The emergence of spin electronics in data storage, *Nat. Mater.*, 2007, **6**, 813.
4 M. C. Prestgard, G. P. Siegel and A. Tiwari, Oxides for Spintronics: A Review of Engineered Materials for Spin Injection, *Adv. Mater. Lett.*, 2014, **5**, 242.
5 X. Li and J. Yang, First-principles design of spintronics materials, *Natl. Sci. Rev.*, 2016, **3**, 365.
6 K. L. Wang, J. G. Alzate and P. K. Amiri, Low-power non-volatile spintronic memory: STT-RAM and beyond, *J. Phys. D: Appl. Phys.*, 2013, **46**, 074003.
7 M. N. Baibich, J. M. Broto, A. Fert, F. N. van Dau, F. Petro, P. Eitenne, G. Creuzet, A. Friederich and J. Chazelas, Giant magnetoresistance of (001) Fe/(001)Cr magnetic superlattices, *Phys. Rev. Lett.*, 1988, **61**, 2472.
8 S. A. Wolf, D. D. Awschalom, R. A. Buhrman, J. M. Daughton, S. V. Molnár, M. L. Roukes, A. Y. Chtchelkanova and D. M. Treger, Spintronics: a spin-based electronics vision for the future, *Science*, 2001, **294**, 1488.
9 J. Puebla, J. Kim, K. Kondou and Y. Otani, Spintronic devices for energy-efficient data storage and energy harvesting, *Commun. Mater.*, 2020, **1**, 24.
10 U. Lüders, A. Barthélémy, M. Bibes, K. Bouzehouane, S. Fusil, E. Jacquet, J. P. Contour, J. F. Bobo, J. Fontcuberta and A. Fert, $NiFe_2O_4$: A Versatile Spinel Material Brings New Opportunities for Spintronics, *Adv. Mater.*, 2006, **18**, 1733–1736.
11 T. S. Santos and J. S. Moodera, Observation of spin filtering with a ferromagnetic EuO tunnel barrier, *Phys. Rev. B: Condens. Matter Mater. Phys.*, 2004, **69**, 241203.
12 J. Moodera, X. Hao, G. Gibson and R. Meservey, Electron -spin polarization in tunnel junctions in zero applied field with ferromagnetic EuS barriers, *Phys. Rev. Lett.*, 1988, **61**, 637.
13 S. Zhe-Wen and L. Bang-Gui, Electronic structure and magnetic and optical properties of double perovskite Bi_2FeCrO_6 from first-principles investigation, *Chin. Phys. B*, 2013, **22**, 047506.
14 J. Wang, J. Meng and Z. Wu, Theoretical insights on the electron doping and Curie temperature in La-doped Sr_2CrWO_6, *J. Comput. Chem.*, 2011, **32**, 3313–3318.
15 E. Şaşıoğlu, L. Sandratskii, P. Bruno and I. Galanakis, Exchange interactions and temperature dependence of magnetization in half-metallic Heusler alloys, *Phys. Rev. B: Condens. Matter Mater. Phys.*, 2005, **72**, 184415.
16 X. Li and J. Yang, First-principles design of spintronics materials, *Natl. Sci. Rev.*, 2016, **3**, 365–381.
17 B. Náfrádi, P. Szirmai, M. Spina, H. Lee, O. Yazyev, A. Arakcheeva, D. Chernyshov, M. Gibert, L. Forró and E. Horváth, Optically switched magnetism in photovoltaic perovskite CH_3NH_3(Mn: Pb) I_3, *Nat. Commun.*, 2016, **7**, 13406.
18 B. Cai, X. Chen, M. Xie, S. Zhang, X. Liu, J. Yang, W. Zhou, S. Guo and H. Zeng, A class of Pb-free double perovskite halide semiconductors with intrinsic ferromagnetism, large spin splitting and high Curie temperature, *Mater. Horiz.*, 2018, **5**, 961.
19 E. Haque and M. A. Hossain, Origin of ultra-low lattice thermal conductivity in Cs_2BiAgX_6 (X= Cl, Br) and its impact on thermoelectric performance, *J. Alloys Compd.*, 2018, **748**, 63.
20 M. Younis Sofi, M. Shahid Khan, J. Ali and M. Ajmal Khan, Unlocking the role of 3*d* electrons on ferromagnetism and spin-dependent transport properties in K_2GeNiX_6 (X = Br, I) for spintronics and thermoelectric applications, *J. Phys. Chem. Solids*, 2024, 112022, DOI: **10.1016/j.jpcs.2024.112022**.
21 P. Blaha, K. Schwarz, G. K. H. Madsen, D. Kvasnicka, J. Luitz, R. Laskowsk, F. Tran, L. Marks and L. Marks, *WIEN2k: An Augmented Plane Wave Plus Local Orbitals Program for Calculating Crystal Properties*, Techn. Universitat, Vienna, Austria, 2019, p. 287.
22 J. P. Perdew, K. Burke and M. Ernzerhof, Generalized gradient approximation made simple, *Phys. Rev. Lett.*, 1996, 77(18), 3865.
23 D. Koller, F. Tran and P. Blaha, Improving the modified Becke–Johnson exchange potential, *Phys. Rev. B: Condens. Matter Mater. Phys.*, 2012, **85**(15), 155109.
24 T. Charpin: A Package for Calculating Elastic Tensors of Cubic Phases Using WIEN: Laboratory of Geometrix F-75252 (Paris, France) (2001).
25 A. tero-de-la-Roza, D. Abbasi-Pérez and V. Luaña, Gibbs2: A new version of the quasi-harmonic model code. II. Models for solid state thermodynamics, features and implementation, *Comput. Phys. Commun.*, 2011, **182**(10), 2232–2248.
26 G. K. Madsen and D. J. Singh, BoltzTraP. A code for calculating band-structure dependent quantities, *Comput. Phys. Commun.*, 2006, **175**(1), 67–71.

27 M. Houari, B. Bouadjemi and A. Abbad, *et al.*, Lead-Free Semiconductors with High Absorption: Insight into the Optical Properties of $K_2GeSnBr_6$ and K_2GeSnI_6 Halide Double Perovskites, *JETP Lett.*, 2020, **112**, 364–369.
28 J. E. Saal, S. Kirklin, M. Aykol, B. Meredig and C. Wolverton, Materials Design and Discovery with High-Throughput Density Functional Theory: The Open Quantum Materials Database (OQMD), *JOM*, 2013, **65**, 1501–1509, DOI: 10.1007/s11837-013-0755-4.
29 P. Giannozzi, *et al.*, QUANTUM ESPRESSO: A modular and open-source software project for quantum simulations of materials, *J. Phys.: Condens. Matter*, 2009, **21**, 395502.
30 M. Blanco, E. Francisco and V. Luaña, GIBBS: isothermal-isobaric thermodynamics of solids from energy curves using a quasi-harmonic Debye model, *Comput. Phys. Commun.*, 2004, **158**, 57–72.
31 Q. Chen and B. Sundman, Calculation of Debye temperature for crystalline structures case study on Ti, Zr, and Hf, *Acta Mater.*, 2001, **49**, 947–961.
32 D. V. Schroeder and J. K. Pribram, An Introduction to Thermal Physics, *Am. J. Phys.*, 1999, **67**, 1284–1285.
33 P. Debye, Zur Theorie der spezifischen Warmen., *Ann. Phys.*, 1912, **344**, 789–839.
34 M. Y. Sofi, M. S. Khan and J. Ali, *et al.*, Exploring the lead-free halide Cs_2MGaBr_6 (M = Li, Na) double perovskites for sustainable energy applications, *Sci. Rep.*, 2024, **14**, 5520.
35 A. T. Petit and P. L. Dulong, Study on the measurement of specific heat of solids, *Ann. Chim. Phys.*, 1819, **10**, 395.
36 M. Born, On the stability of crystal lattices, *Math. Proc. Cambridge Philos. Soc.*, 1940, **36**, 160.
37 W. Voigt, in *Textbook of Crystal Physics*, ed. G. B. Teubner, 1928.
38 A. Reuss, Berechnung Der Fließgrenze von Mischkristallen Auf Grund Der Plastizitätsbedingung Für Einkristalle, *Z. Angew. Math. Mech.*, 1929, **9**, 49–58.
39 R. Hill, Te elastic behaviour of a crystalline aggregate, *Proc. Phys. Soc., London, Sect. A*, 1952, **65**, 349.
40 M. Y. Sofi and D. C. Gupta, Scrutinized the inherent spin half-metallicity and thermoelectric response of f-electron-based $RbMO_3$ (M = Np, Pu) perovskites: a computational assessment, *Sci. Rep.*, 2022, **12**, 19476.
41 S. F. Pugh, XCII. Relations between the elastic moduli and the plastic properties of polycrystalline pure metals, *Philos. Mag.*, 1954, **45**, 823–843.
42 I. N. Frantsevich; F. F. Voronov and S. A. Bakuta, Elastic Constants and Moduli of Elasticity of Metals and Nonmetals, Naukova Dumka: Kiev, 1982.
43 W. Hume-rothery, Elasticity and anelasticity of metals, *Nature*, 1949, **164**(4159), 84–85.
44 S. I. Ranganathan and M. Ostoja-Starzewski, Universal elastic anisotropy index, *Phys. Rev. Lett.*, 2008, **101**(5), 055504.
45 D. M. Teter, Computational alchemy: The search for new superhard materials, *MRS Bull.*, 1998, **23**(1), 22–27.
46 Y. Tian, B. Xu and Z. Zhao, Microscopic theory of hardness and design of novel superhard crystals, *Int. J. Refract. Met. Hard Mater.*, 2012, **33**, 93–106.
47 E. Fine, L. D. Brown and H. L. Marcus, Elastic constants versus melting temperature in metals, *Scr. Metall.*, 1984, **18**, 951–956.
48 H. Yilin, W. Yang, L. Tingzhou, Y. Tie and W. Xiaotian, Electronic, magnetic, half-metallic, and mechanical properties of a new equiatomic quaternary Heusler compound YRhTiGe: a first-principles study, *Materials*, 2018, **11**, 797.
49 M. Y. Sofi, M. S. Khan, J. Ali and M. Ajmal Khan, in Novel Thermoelectric Material Ba_2AlNbO_6 for Energy Harvesting Applications, ed. Khan, Z. H., Jackson, M., Salah, N. A., *Recent Advances in Nanotechnology, ICNOC 2022, Springer Proceedings in Materials*, Springer, 2023, vol 28, Singapore, pp. 85–91.
50 M. Jonson and G. D. Mahan, Mott's formula for the thermopower and the Wiedemann-Franz law, *Phys. Rev. B: Condens. Matter Mater. Phys.*, 1980, **21**, 4223–4229.
51 P. Nath, *et al.*, High throughput combinatorial method for fast and robust prediction of lattice thermal conductivity, *Scr. Mater.*, 2017, **129**, 88–93.
52 Y. Ouyang, Z. Zhang, D. Li, J. Chen and G. Zhang, Emerging theory, materials, and screening methods: New opportunities for promoting thermoelectric performance, *Ann. Phys.*, 2019, **531**, 1800437.
53 C. W. Wu, X. Ren, G. Xie, W. X. Zhou, G. Zhang and K. Q. Chen, Enhanced High-Temperature Thermoelectric Performance by Strain Engineering in BiOCl, *Phys. Rev. Appl.*, 2022, **18**(1), 014053.